SANDIA REPORT
SAND2019-2097
Printed February 2019

Sandia National Laboratories

Dynamic Tensile Characterization of Hiperco 50A Alloy at Various Strain Rates and Temperatures

Bo Song, Brett Sanborn

Prepared by
Sandia National Laboratories
Albuquerque, New Mexico
87185 and Livermore,
California 94550

Issued by Sandia National Laboratories, operated for the United States Department of Energy by National Technology & Engineering Solutions of Sandia, LLC.

Available to DOE and DOE contractors from
U.S. Department of Energy
Office of Scientific and Technical Information
P.O. Box 62
Oak Ridge, TN 37831

Telephone: (865) 576-8401
Facsimile: (865) 576-5728
E-Mail: reports@osti.gov
Online ordering: http://www.osti.gov/scitech

Available to the public from
U.S. Department of Commerce
National Technical Information Service
5301 Shawnee Rd
Alexandria, VA 22312

Telephone: (800) 553-6847
Facsimile: (703) 605-6900
E-Mail: orders@ntis.gov
Online order: https://classic.ntis.gov/help/order-methods/

ABSTRACT

Soft ferromagnetic alloys are often utilized in electromagnetic applications due to their desirable magnetic properties. In support of these applications, the ferromagnetic alloys are also desired to bear mechanical load at various environmental temperatures. In this study, a Permendur 2V alloy manufactured by Metalwerks Inc. (but referred to Hiperco 50A, a trademark of Carpenter Technologies Inc.) was dynamically characterized in tension with a Kolsky tension bar and a Dropkinson bar at various strain rates and temperatures. Dynamic tensile stress-strain curves of the Hiperco 50A alloy were obtained at the strain rates ranging from 40 to 230 s^{-1} and temperatures from -100 to 100°C. All tensile stress-strain curves exhibited an initial linear elastic response to an upper yield followed by a Lüders banding response and then a nearly linear work-hardening behavior. The yield strength of this material was found to be sensitive to both strain rate and temperature; whereas, the hardening rate was independent of strain rate or temperature. The Hiperco 50A alloy exhibited a feature of brittle fracture in tension under dynamic loading with no necking being observed.

ACKNOWLEDGEMENTS

The authors acknowledge Kyle Johnson, Jefferey Dabling, Donald Susan, Jay Carroll, Adam Brink, Scott Grutzik, and Andrew Kustas for the valuable discussion of test plan and results. Thanks Donald Susan for specimen preparation for this project.

The authors also thanks Randy Everett for his support to the operation of dynamic tests in this project.

CONTENTS

LIST OF FIGURES

LIST OF TABLES

ACRONYMS AND DEFINITIONS

Abbreviation	Definition

This page left blank

1. INTRODUCTION

Soft ferromagnetic alloys are often utilized in electromagnetic applications due to their desirable magnetic properties. Fe-49Co-2V is an example of one of these alloys to which attention has been recently paid for use in magnetic bearings and electrical generators. In support of these applications, the ferromagnetic alloys are also desired to bear mechanical load at various environmental temperatures. The mechanical properties of Fe-49Co-2V alloy have thus been quasi-statically characterized at various temperatures. For example, Ren et al. [1] investigated mechanical properties of Fe-49Co-2V in tension within quasi-static strain rate regime at temperatures from room temperature to 800°C. Generally, the Fe-49Co-2V possessed an elastic response followed by a yield, plastic plateau, and then a significant work-hardening behavior in tension. Their results also showed that the Fe-49Co-2V alloy exhibited significant strain rate effect, even within the quasi-static regime, and temperature effect [1]. The yield/plateau strength increased with increasing strain rate. When temperature was below 300°C, the yield/plateau strength decreased with increasing temperature. However, when temperature was between 300 and 700°C, such a temperature effect diminished. By contrast to strain-rate and temperature effects on the yield/plateau strength, the work-hardening rate for the Fe-49Co-2V did not show significant strain rate or temperature effect until temperature reached 800°C. The yield strength of the material was also concluded to significantly depend on grain size following a Hall-Petch relationship. Duckham et al. [2] also quasi-statically investigated temperature dependent tensile properties of ultra-fine grained Fe-49Co-2V alloy. As temperature increased from room temperature up to 400°C, the yield strength decreased and ductility increased from between 3-13% at room temperature to ~22% at 400°C. They also observed that the work-hardening rate decreased with increasing temperature. It was concluded that grain boundary strengthening, which is inversely dependent of grain size due to Hall-Petch relationship, was highly effective in producing extremely high yield strength for temperatures ranging from room temperature to about 400°C [2]. The grain size was found to significantly affect the plastic flow behavior of the material. The specimens with a grain size of 290 nm, in comparison to the specimens with grain sizes of 100 and 150 nm, showed the most distinct yield point followed by Lüders banding up to 6% strain and then a linear work hardening [2]. The Fe-49Co-2V alloy also exhibited significant uniaxial anisotropic mechanical and magnetic behavior which can be reduced by annealing [3-5].

As of today, the Fe-49Co-2V alloy has only been mechanically characterized under quasi-static loading conditions. Furthermore, the Fe-49Co-2V alloy has only been characterized at high temperatures rather than low temperatures. However, in applications, the components made of the Fe-49Co-2V alloy may be subjected to abnormal mechanical environments such as accidental drop or low-speed impact and different (low or high) temperatures. Due to strain-rate effect discovered by Ren et al. [1], the mechanical properties of the Fe-49Co-2V under impact loading conditions, even at relatively low impact velocities, may significantly change. However, there is no such dynamic experimental data available for this material. Temperature may also influence the dynamic properties of the material; however, no experimental data is available. In this study, we dynamically characterize the Fe-49Co-2V alloy in tension at moderate impact speeds (strain rates) and different temperatures.

This page left blank

2. EXPERIMENTAL SETUP

Dynamic tensile tests were conducted with a Kolsky tension bar and a newly developed Dropkinson (also called Drop-Hopkinson) bar [6] at Sandia National Laboratories.

2.1. Conventional Kolsky Tension Bar

The Kolsky tension bar is schematically shown in Figure 2-1. In this design, a solid cylindrical striker is launched to impact an end cap attached to the open end of a gun barrel [7]. This design enables direct application of pulse shaping methods used in a Kolsky compression bar to the tension bar. Compared to other Kolsky tension bar designs, the gun barrel in this design acts as a portion of load transfer train. Upon the impact of striker on the pulse shaper placed on the end cap, a shaped tensile stress wave is generated in the gun barrel and then transfers into the incident bar that is attached to the other end of the gun barrel through a coupler. The tensile wave then propagates in the incident bar and is recorded as an "incident wave" with a pair of strain gages on the incident bar. Upon reaching the specimen interface, the specimen, which is threaded into the ends of the incident and transmission bars, is loaded in tension whereupon part of the incident pulse is reflected back into the incident bar, as a "reflected wave", and the rest transmits into the transmission bar, as a "transmitted wave", recorded with another pair of strain gages on the transmission bar. In this study, both incident and transmission bars were made of C300 maraging steel and had a common diameter of 1". A pair of lock nuts was used between the threads of the tensile specimen and the bar ends. The lock nuts produced a tight connection between the tensile specimen and the bar ends without generating any pre-tension or torque to the specimen gage section [8-11]. This method minimizes the wave distortion caused by the threads [12].

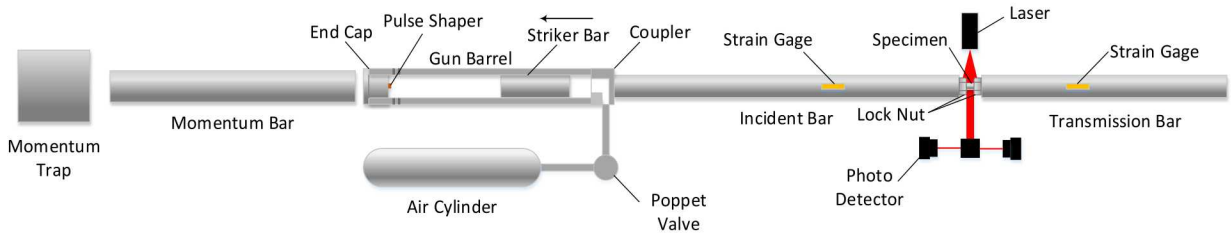

Figure 2-1. A Schematic of Kolsky Tension Bar

A high-speed dual photodetector linear laser extensometer system was placed at the specimen section to simultaneously track the motions of the incident bar/specimen and specimen/transmission bar interfaces (Figure 2-1) [11, 13]. The laser extensometer therefore measures the total displacement over the tensile specimen. Since the tensile specimen has a dog-bone shape and the displacement is measured between the shoulders of the specimen, the measured displacement includes the displacements over both gage and shoulder sections. The specimen strain over gage section needs to be corrected with the total displacement using the output of the incident and transmission bar detectors [8-10],

$$\varepsilon(t) = c' \cdot \frac{L_1(t) - L_2(t)}{L_s} \tag{2.1}$$

where L_1 and L_2 are the displacements at the incident bar/specimen and specimen/transmission bar interfaces, respectively; L_s is the gage length of the tensile specimen; c' is correction factor. The determination of the correction factor, c', will be presented in Section 3.3. The time derivative of Equation (2.1) yields strain rate in the specimen.

The specimen strain rate and strain histories can also be calculated with the conventional method using strain-gage signals [14],

$$\dot{\varepsilon}(t) = c' \cdot \frac{2\varepsilon_r(t)}{L_s} \cdot C_0 \tag{2.2}$$

$$\varepsilon(t) = c' \cdot \int_0^t \frac{2\varepsilon_r(t)}{L_s} \cdot C_0 dt \tag{2.3}$$

where ε_r is the reflected strain recorded with the strain gages on the incident bar; C_0 is the elastic wave speed in the bar material, $C_0 = 4870\,\text{m/s}$ for C300 maraging steel. Similar to the laser extensometer measurement, the conventional method also measures the displacements for both gage and shoulder sections. The same specimen strain correction factor, c', applies.

In this study, the laser extensometer method (Equation (2.1)) was used for all room-temperature tests; while the strain-gage method (Equation (2.3)) was used for all high/low-temperature tests where an environmental chamber prevented the use of the laser extensometer system. However, attention needs to be paid when using strain-gage signals (Equation (2.3)) to calculate the specimen strain since the reflected strain signal may be distorted due to threads. Only after the pre-torque is applied to the lock nuts above a threshold value, does the distortion effect of the reflected wave signal become negligible. In this study, a pre-torque of 12.43 N-m (110 in-lbs) was applied to the lock nuts.

The specimen stress history is calculated with the transmitted strain signal, ε_t, recorded with the strain gages on the transmission bar [14],

$$\sigma(t) = E_0 \cdot \varepsilon_t(t) \cdot \frac{A_0}{A_s} \tag{2.4}$$

where E_0 is Young's modulus for the bar material, $E_0 = 189.7$ GPa for C300 maraging steel; A_0 and A_s are cross-sectional areas of the bars and specimen, respectively. Synchronizing the stress (Equation (2.4)) and strain histories (Equation (2.1) or (2.3)) yields a tensile stress-strain curve.

2.2. Dropkinson Bar

The conventional Kolsky bar presented in 2.1 usually has a limited duration of loading, which depends on the lengths of striker, incident and transmission bars. For the Kolsky tension bar in this study, the loading duration was limited to 0.5 ms. This limitation of loading duration results in a limit of maximum strain produced in the specimen. For example, for a total loading duration of 0.5 ms, the specimen strain achieved during the experiment is only 2.5% at a strain rate of 50 s^{-1}. Therefore, a newly developed Dropkinson bar was employed to conduct dynamic tensile tests at lower rates [15, 16]. The Dropkinson bar can generate a loading duration of 1.35 ms, which produces a strain of 6.75% at the same strain rate of 50 s^{-1}.

The photograph of the actual Dropkinson bar is shown in Figure 2-2 [16].

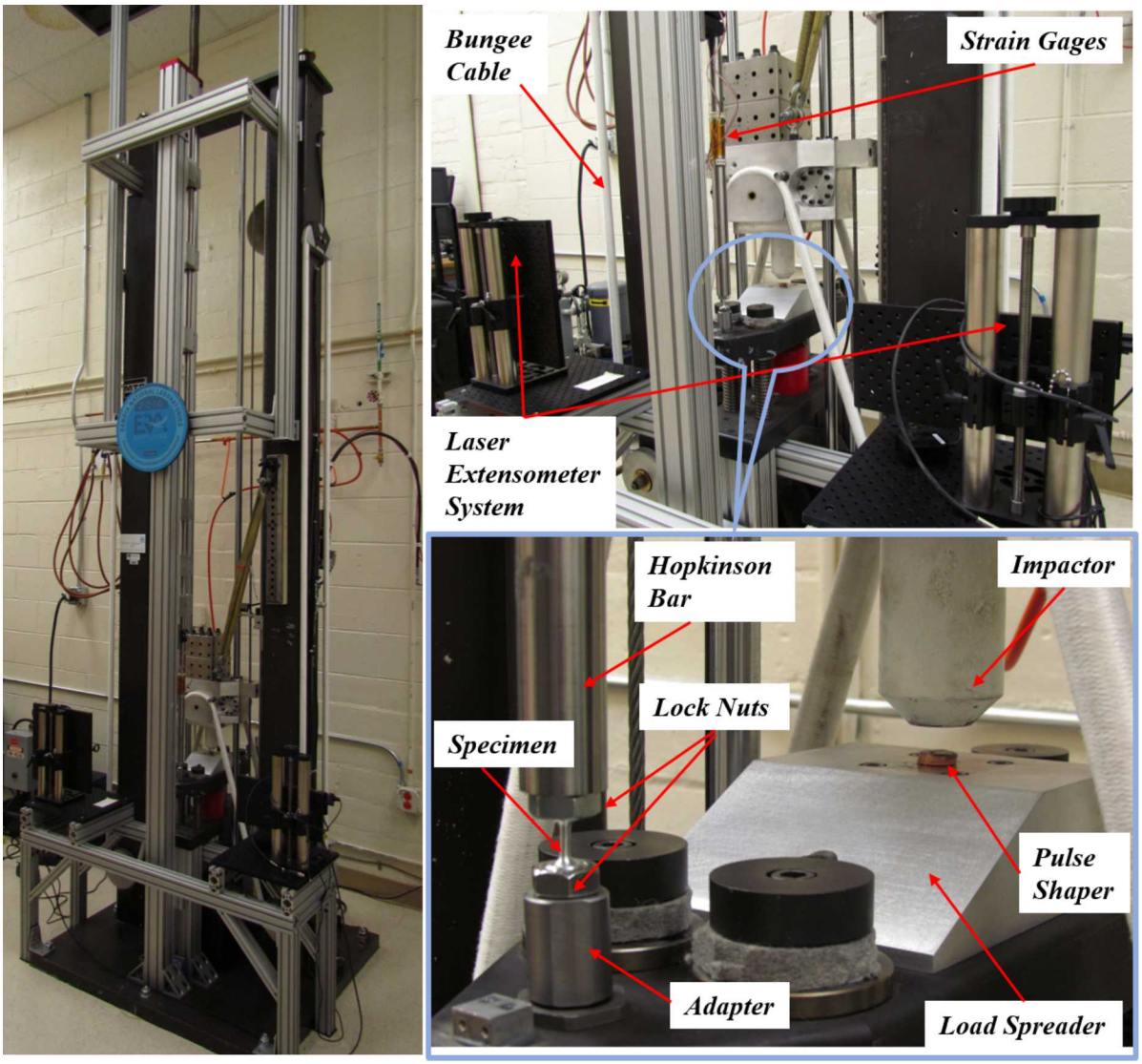

Figure 2-2. Photographs of Dropkinson Bar

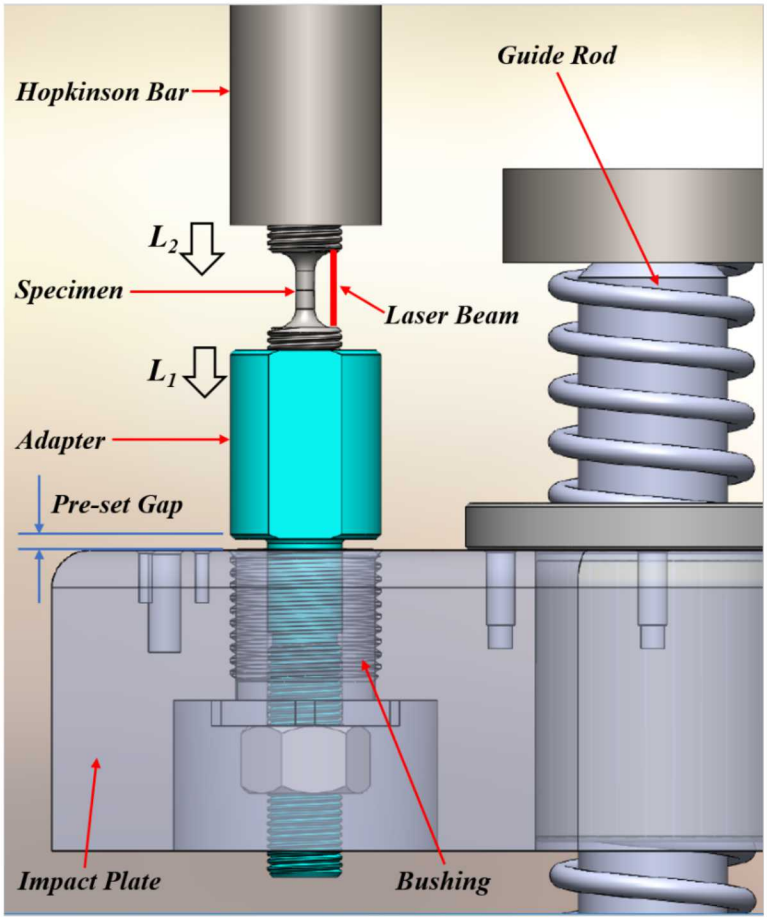

Figure 2-3. Illustration of Tensile Specimen Attached to the Dropkinson Bar

As seen in Figure 2-2, a 50.4-mm-diameter cylindrical steel impactor with a tapered impact end of 25.4-mm in diameter was attached to the bottom of the carriage to strike the center of an impact plate through a load spreader. A pulse shaper was placed on the top of the load spreader to generate a desired loading pulse profile (Figure 2-2), similar to a Kolsky bar test [5]. The load spreader significantly minimized the bending wave generated by the impactor. A 50.8-mm-thick, 25-kg, impact plate, made of solid hardened 4340 steel, was mounted on several guide rods to ensure downward motion of the plate with minimal bending effect. Springs were installed, surrounding the guide rods and between the impact plate and bottom plate, to support the impact plate. A bushing was mounted in the hole in the impact plate to the left of the guide rods to facilitate tensile specimen attachment via an adapter as shown in Figure 2-3. The adapter had a ½"-20 female thread on the top and the same size male thread on the bottom. The tensile specimen was threaded into the top part of the adapter. The bottom male thread of the adapter passed through the bushing installed on the impact plate and was locked against the bottom of the bushing with a nut (Figure 2-3). Also shown in Figure 2-3, a small gap was pre-set between the adapter and the impact plate before test. This gap allows only tensile force be transferred to the specimen and prevented any possible pre-compression caused by the bending of the impact plate from being transferred to the specimen. The other end of the tensile specimen was threaded into the ½"-20 female threaded end of the 25.4-mm-

diameter Hopkinson bar. Similar to a conventional Kolsky tension bar presented in 2.1, the specimen was also locked to the Hopkinson bar and the adapter attached to the impact plate via a pair of lock nuts (not shown in Figure 2-3). A pair of strain gages was attached on the surface of the Hopkinson bar to record the load history in the tensile specimen (Figure 2-2). On the top end of the Hopkinson bar, a long spring was installed to suspend the Hopkinson bar to compensate the gravity of the Hopkinson bar that may compress the tensile specimen before dynamic tensile loading.

Upon the drop of the carriage, the impactor attached to the bottom of the carriage impacts the load spreader via a pulse shaper and transfers the impact load to the impact plate. The whole impact plate then moves downwards to pull the tensile specimen attached between the impact plate and the Hopkinson bar. Such an impact event generates a dynamic tensile stress wave with a duration on the order of milliseconds. The tensile stress wave then transmits into the vertical Hopkinson bar through the specimen and propagates upwards to the top free end of the Hopkinson bar. The current 3657-mm-long Hopkinson bar can accommodate an impact pulse with a duration up to 1.35 ms without wave overlap. When pulse shaping and short-gage-length specimens are used at intermediate rates, specimen stress equilibrium is more easily achieved than at high-strain-rates due to lower inertia. The specimen stress can be calculated with Equation 2.4. The laser extensometer system presented in 2.1 was also implemented on the Dropkinson bar for specimen displacement measurement. The specimen strain can be calculated with Equation 2.1.

2.3. Environmental Chamber

In this study, an Instron environmental chamber was used with the conventional Kolsky tension bar for dynamic tensile tests at various temperatures, as shown in Figure 2-4. The chamber has a temperature range from -100 to 350°C. As shown in Figure 2-4, the chamber covered the testing section of the Kolsky tension bar. The specimen that was threaded to the bar ends was pre-conditioned to the desired temperature prior to dynamic loading. In this study, the material was dynamically characterized at four temperatures: -100, -50, 20 (room temperature), and 100°C. The temperatures of interest in this study are considered to generate negligible temperature effect on the mechanical properties, i.e., Young's modulus, of the bars such that no additional correction of bar properties was needed.

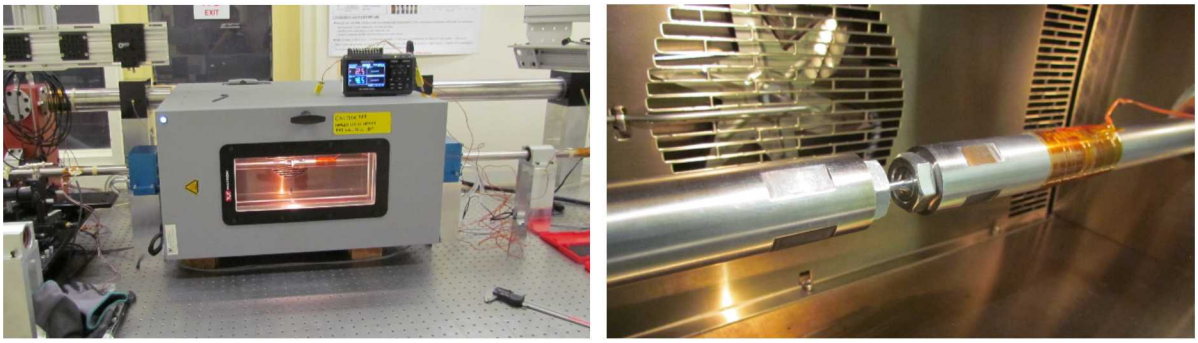

Figure 2-4. Environmental Chamber for the Kolsky Tension Bar

This page left blank

3. EXPERIMENTAL PROCEDURE AND DATA REDUCTION

3.1. Material and Specimen

In this study, the material under investigation was manufactured by Metalwerks Inc. Note the alloy is called Permendur 2V but will be referred to as Hiperco 50A below (Hiperco is a tradename of Carpenter Technologies Inc.). The measured alloy composition was: 49.1 wt.% Co, 1.93 wt.% V, 0.051 wt.% Nb and balance Fe. The slight Nb addition was intended to promote grain refinement during processing but is not expected to significantly affect behavior in dynamic testing. This particular type of Hiperco was previously characterized in quasi-static room temperature tensile testing [17]. The Hiperco bar was manufactured by gyrotory forging to 2 in. and 1 in. diameters. The test specimens for this study were machined in the longitudinal orientation from 2 in. diameter bar. After machining, all specimens were heat treated at 838°C for 2 hours to impart good magnetic behavior and simulate the material condition used in component applications.

The Hiperco 50A alloy was made into cylindrical specimens with a dog-bone shape, as illustrated in Figure 3-1(a). The cylindrical tensile specimens had a gage section that was 3.18 mm in diameter and 6.35 mm long. The tensile specimens had ½"-20 male threads at both ends so as to be directly threaded into the bars, as shown in Figure 3-1(b). Figure 3-1(b) also shows the lock nuts applied to the specimen against the bars.

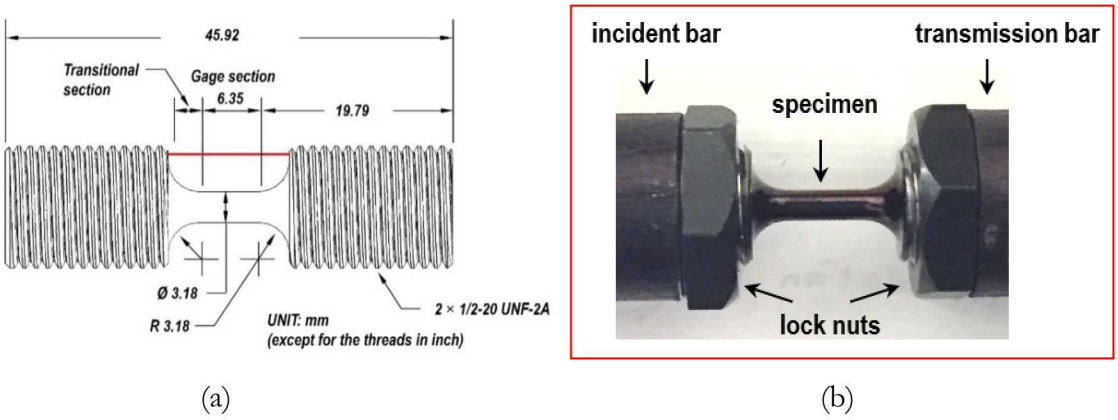

Figure 3-1. Specimen Design and Installation

3.2. Experiments

In this study, the Hiperco 50A was characterized with conventional Kolsky tension bar and Dropkinson bar at various strain rates and temperatures. Detailed testing conditions are summarized in Table 3-1.

Table 3-1. Testing Apparatus and Conditions

Nominal Strain Rate (s^{-1})	Temperature (C)	Apparatus	Loading Condition	Pulse Shaper
220	20 (Room Temperature)	Kolsky Tension Bar	1.524-m-long striker Air pressure: 100 psi	Ø4.775 mm × 3.429 steel
220	100	Kolsky Tension Bar	1.524-m -long striker Air pressure: 100 psi	Ø4.775 mm × 3.429 steel
220	-100	Kolsky Tension Bar	1.524-m -long striker Air pressure: 100 psi	Ø4.775 mm × 3.429 steel
230	-50	Kolsky Tension Bar	1.524-m -long striker Air pressure: 100 psi	Ø4.775 mm × 3.429 steel
65	-100	Kolsky Tension Bar	1.524-m -long striker Air pressure: 15 psi	Ø4.775 mm × 3.429 steel
110	20 (Room Temperature)	Dropkinson Bar	Drop height: 0.267 m	Ø12.700 mm × 4.775 mm copper
40	20 (Room Temperature)	Dropkinson Bar	Drop height: 0.267 m	Ø12.700 mm × 4.775 mm copper

Figure 3-2(a) shows a typical set of original records of strain-gage signals during a conventional Kolsky tension bar test at room temperature. The incident pulse was quite different from a classic square pulse, which is the result of utilization of pulse shapers listed in Table 3-1. Such a modified incident pulse is necessary to facilitate a constant strain rate deformation of the specimen. Also shown in Figure 3-2(a), the reflected pulse was overlapped with the unloading portion of the incident pulse since a long (~0.7 ms) pulse of loading was needed to generate a relatively large deformation at a moderate strain rate (~220 s^{-1}). As such, the reflected pulse could not be used to calculate the strain rate and strain in the specimen with Equations (2.2) and (2.3). Instead, the laser extensometer signal shown in Figure 3-2(b) was used to calculate the specimen strain (Equation (2.1)) and strain rate. As seen in Figure 3-2(b), the incident bar end shows a larger displacement than the transmission bar end, meaning that the specimen was dynamically elongated. However, as discussed earlier, such an elongation was applied to not only the gage section but also specimen shoulders, which needs to be corrected.

The transmitted signal shown in Figure 3-2(a) represents the specimen stress history. From the transmitted signal, the material showed an initial elastic response followed by an upper yield and then a significant hardening behavior. The ultimate strength is nearly double of the yield. Such a hardening response invalidates the currently existing specimen strain correction method.

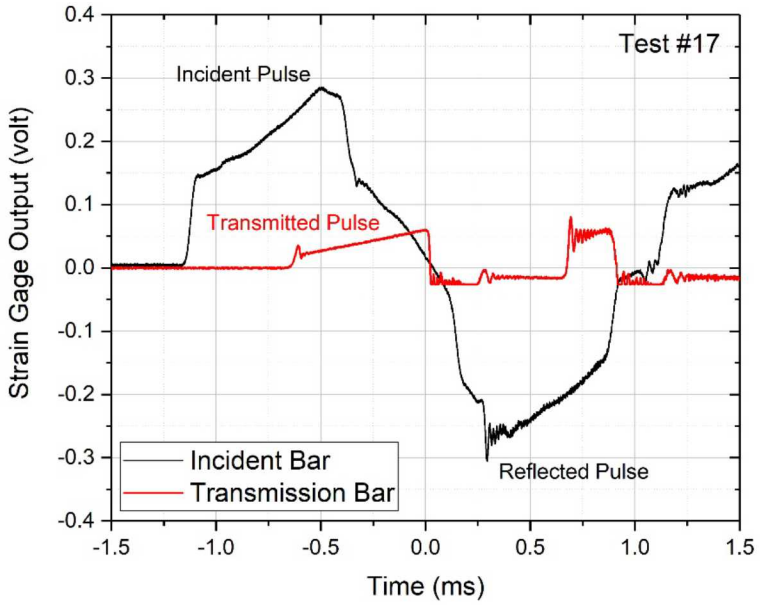

(a) Strain Gage Signals

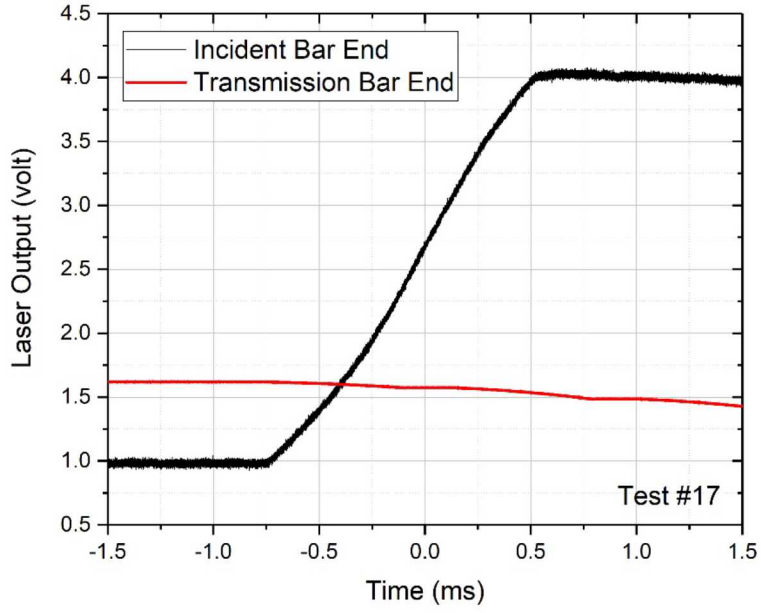

(b) Laser Extensometer Signals

Figure 3-2. Original Strain Gage and Laser Extensometer Signals

3.3. Specimen Strain Correction

In a Kolsky tension bar, a specimen strain correction method has been previously developed. However, the currently available correction method is based on an elastic-perfectly plastic response. This assumption ensures the specimen shoulders are always in elasticity while the gage section keeps being elongated into plasticity [8-10]. This is obviously not applicable to the Hiperco 50A alloy that exhibits significant work-hardening behavior. Therefore, a new specimen strain correction method needs to be developed for elastic-work-hardening materials, i.e., Hiperco 50A.

In this study, we developed a new correction method for Hiperco 50A based on a stress-strain response of elastic-linear-hardening with high yield point, as illustrated in Figure 3-3. As shown in Figure 3-3, the stress-strain response was divided into three regions:

Region I: elasticity region when $\sigma < \sigma_{y1}$ or $F < F_{y1}$. In this region, both gage section and shoulders are in elasticity.

Region II: post-yield region (Lüders band) when $\sigma_{y2} < \sigma < \sigma_{y1}$ or $F_{y2} < F < F_{y1}$. In this region, the gage section is in plasticity while the shoulders remain in elasticity.

Region III: work-hardening region when $\sigma > \sigma_{y1}$ or $F > F_{y1}$. In this region, the gage section is in plasticity and a portion of the shoulders is in plasticity.

where σ_{y1} and σ_{y2} are be upper and lower yield strengths, respectively.

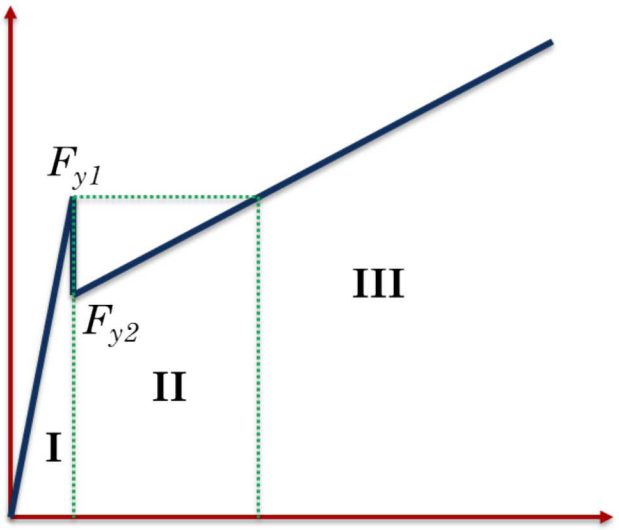

Figure 3-3. Simplified Model for Specimen Strain Correction

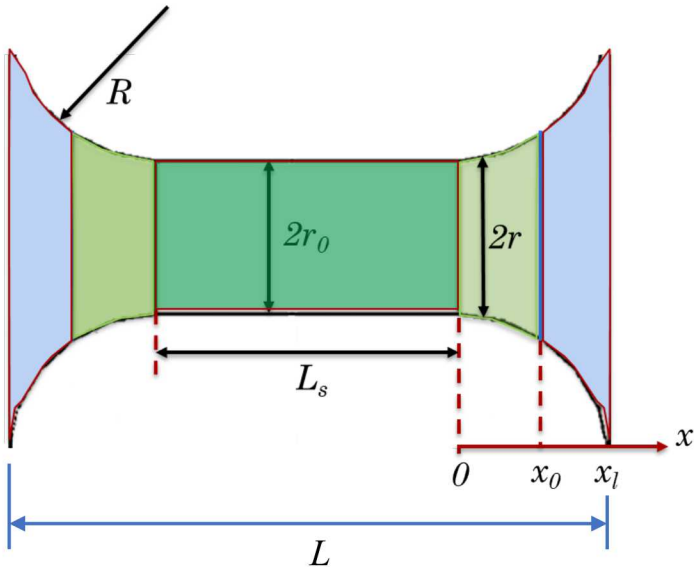

Figure 3-4. Illustration of Specimen Gage and Shoulder Sections

In *Region I*, since the specimen is subjected to linearly elastic deformation, the previous analysis for specimen strain correction is still valid. The correction factor, c', can be calculated with

$$c' = \frac{\Delta L_s}{\Delta L + \Delta L_s} \tag{3.1}$$

where ΔL and ΔL_s are the displacements in the shoulder (non-gage) and gage sections, respectively, when the specimen is subjected to a common force, *F*. For the specimen geometry shown in Figure 3-4, we have

$$\Delta L = 2\int_0^{x_l} \frac{F}{E_s \pi \left(R + r_0 - \sqrt{R^2 - x^2}\right)^2} dx = 2 \cdot \frac{F}{E_s \pi} \cdot \int_0^{x_l} \frac{dx}{\left(R + r_0 - \sqrt{R^2 - x^2}\right)^2} \tag{3.2}$$

$$\Delta L_s = \frac{F}{E_s \pi} \cdot \frac{L_s}{r_0^2} \tag{3.3}$$

where E_s is Young's modulus of the specimen material. Substitution of Equations (3.2) and (3.3) into (3.1) yields

$$c' = \frac{1}{1 + 2 \cdot \frac{r_0^2}{L_s} \cdot \int_0^{x_l} \frac{dx}{\left(R + r_0 - \sqrt{R^2 - x^2}\right)^2}}$$

(3.4)

For the specimen dimensions used in this study, as shown in Figure 3-1(a), $r_0 = 1.59$ mm, $x_l = R = 3.18$ mm, and $L_s = 6.35$ mm, the specimen strain correction factor, c', for the *Region I*, is a constant, $c' = 0.62$.

In *Region II*, the shoulders (non-gage section) are always in elasticity. The displacement over the shoulders can still be calculated with Equation (3.2). However, the specimen gage-section is in a state of uniform plasticity. The displacement over the gage section consists of elastic-to-yield (ε_y) and plastic (ε_p) deformation,

$$\Delta L_s = \varepsilon \cdot L_s$$

(3.5)

The total displacement is the sum of the displacements over the gage section and the shoulders,

$$L_1 - L_2 = \Delta L + \Delta L_s = \Delta L + \varepsilon \cdot L_s$$

(3.6)

The strain over gage section is

$$\varepsilon = \frac{L_1 - L_2}{L_s} - \frac{\Delta L}{L_s}$$

(3.7)

Applying Equation (3.2) to (3.7) we have

$$\varepsilon = \frac{L_1 - L_2}{L_s} - \frac{2F}{E_s \pi L_s} \int_0^{x_l} \frac{dx}{\left(R + r_0 - \sqrt{R^2 - x^2}\right)^2}$$

(3.8)

Considering Equation (3.2), Equation (3.8) can be rewritten as

$$\varepsilon = \frac{L_1 - L_2}{L_s} - \frac{F}{E_s \pi r_0^2}\left(\frac{1}{c'} - 1\right) = \frac{L_1 - L_2}{L_s} - \frac{\sigma}{E_s}\left(\frac{1}{c'} - 1\right)$$

(3.9)

Therefore, after the total displacement ($L_1 - L_2$) and applied force (F) or stress (σ) are measured, the specimen strain over gage section in *Region II* can be calculated. In Equation (3.9), E_s is Young's modulus of the specimen material which can be determined from the stress-strain response in *Region I*.

When the applied force is larger than F_{y1} ($F > F_{y1}$) or the stress is higher than the upper yield strength σ_{y1} ($\sigma > \sigma_{y1}$), the shoulder sections progress toward plasticity (*Region III*). There exists a

boundary ($x = x_0$ in Figure 3-4) dividing the shoulder sections into two regions: elastic region ($x_0 < x \le x_l$) and plastic region ($0 \le x < x_0$). In this case, the boundary $x = x_0$ moves outwards while the applied force increases, meaning that x_0 is a function of applied force F. Since yielding occurs at $x = x_0$,

$$\sigma\big|_{x=x_0} = \sigma_{y1} = \frac{F_{y1}}{\pi r_0^2}$$

(3.10)

we have

$$\frac{F}{\pi r^2\big|_{x=x_0}} = \frac{F_{y1}}{\pi r_0^2}$$

(3.11)

From Figure 3-4, we have

$$r(x) = R + r_0 - \sqrt{R^2 - x^2}$$

(3.12)

or

$$r(x)\big|_{x=x_0} = R + r_0 - \sqrt{R^2 - x_0^2} \tag{3.13}$$

Equation (3.11) can be rewritten as

$$\frac{F}{\left(R + r_0 - \sqrt{R^2 - x_0^2}\right)^2} = \frac{F_{y1}}{r_0^2}$$

(3.14)

which has the following solution of x_0

$$x_0 = r_0\sqrt{\left(\sqrt{\frac{F}{F_{y1}}} - 1\right)\cdot\left[2\cdot\frac{R}{r_0} - \left(\sqrt{\frac{F}{F_{y1}}} - 1\right)\right]}$$

(3.15)

For the elastic region in the shoulder section $x_0 < x \le x_l$, the total displacement is calculated as

$$\Delta L_1 = 2\cdot\frac{F}{E_s\pi}\cdot\int_{x_0}^{x_l}\frac{dx}{\left(R + r_0 - \sqrt{R^2 - x^2}\right)^2}$$

(3.16)

For the plastic region in the shoulder section $0 \le x < x_0$, the total displacement is calculated as

$$\Delta L_2 = \Delta L_{2e} + \Delta L_{2p}$$
(3.17)

where ΔL_e and ΔL_p are displacements contributing to elastic deformation to yield and plastic deformation, respectively. The displacement for elastic deformation to yield is

$$\Delta L_{2e} = 2\int_0^{x_0} \varepsilon_y dx = 2 \cdot \varepsilon_y \cdot x_0$$
(3.18)

where the yield strain ε_y is determined as

$$\varepsilon_y = \frac{F_{y1}}{E_s \pi r_0^2} = \frac{\sigma_{y1}}{E_s}$$
(3.19)

The displacement for plastic deformation is

$$\Delta L_{2p} = 2\int_0^{x_0} \varepsilon_p dx$$
(3.20)

For a material with a linear hardening response shown in Figure 3-3, the plastic strain ε_p is

$$\varepsilon_p = \frac{\sigma - \sigma_{y2}}{E_p} = \frac{F - \sigma_{y2} \cdot \pi \cdot r^2}{E_p \cdot \pi \cdot r^2}$$
(3.21)

where E_p is modulus of hardening; r is a function of x as expressed in Equation (3.12). Substitution of Equation (3.21) into (3.20) yields

$$\Delta L_{2p} = \frac{2}{E_p} \cdot \left[\frac{F}{\pi} \cdot \int_0^{x_0} \frac{dx}{\left(R + r_0 - \sqrt{R^2 - x^2}\right)^2} - \sigma_{y2} \cdot x_0 \right]$$
(3.22)

Therefore, the total displacement over the shoulders (non-gage sections) can be expressed as

$$\Delta L = \Delta L_1 + \Delta L_{2e} + \Delta L_{2p}$$
$$= \frac{2 \cdot F}{E_s \cdot \pi} \cdot \int_{x_0}^{x_l} \frac{dx}{\left(R + r_0 - \sqrt{R^2 - x^2}\right)^2} + \frac{2 \cdot x_0}{\pi \cdot r^2}\left(\frac{F_{y1}}{E_s} - \frac{F_{y2}}{E_p}\right) + \frac{2 \cdot F}{E_p \cdot \pi} \cdot \int_0^{x_0} \frac{dx}{\left(R + r_0 - \sqrt{R^2 - x^2}\right)^2}$$
(3.23)

The displacement over the gage section is

$$\Delta L_s = L_s\left(\varepsilon_y + \varepsilon_p\right)$$
(3.24)

The total displacement for both gage section and shoulders is

$$L_1 - L_2 = L_s\left(\varepsilon_y + \varepsilon_p\right) + \frac{2\cdot F}{E_s\cdot\pi}\cdot\int_{x_0}^{x_l}\frac{dx}{\left(R + r_0 - \sqrt{R^2 - x^2}\right)^2} + \frac{2\cdot x_0}{\pi\cdot r^2}\left(\frac{F_{y1}}{E_s} - \frac{F_{y2}}{E_p}\right) + \frac{2\cdot F}{E_p\cdot\pi}\cdot\int_0^{x_0}\frac{dx}{\left(R + r_0 - \sqrt{R^2 - x^2}\right)^2} \tag{3.25}$$

From Equation (3.21), we have

$$E_p = \frac{F - \sigma_{y2}\cdot\pi\cdot r_0^2}{\varepsilon_p\cdot\pi\cdot r_0^2} \tag{3.26}$$

Equation (3.25) can thus be rewritten as

$$L_1 - L_2 = L_s\left(\varepsilon_y + \varepsilon_p\right) + \frac{2\cdot x_0\cdot F_{y1}}{\pi\cdot r^2\cdot E_s} - \frac{2\cdot\sigma_{y2}\cdot x_0\cdot\varepsilon_p\cdot\pi\cdot r_0^2}{F - \sigma_{y2}\cdot\pi\cdot r_0^2} + \frac{2\cdot F}{E_s\cdot\pi}\cdot\int_{x_0}^{x_l}\frac{dx}{\left(R + r_0 - \sqrt{R^2 - x^2}\right)^2} + \frac{2\cdot F\cdot\varepsilon_p\cdot r_0^2}{F - \sigma_{y2}\cdot\pi\cdot r_0^2}\cdot\int_0^{x_0}\frac{dx}{\left(R + r_0 - \sqrt{R^2 - x^2}\right)^2} \tag{3.27}$$

The gage-section plastic strain ε_p is thus

$$\varepsilon_p = \frac{L_1 - L_2 - \frac{2\cdot F}{E_s\cdot\pi}\cdot\int_{x_0}^{x_l}\frac{dx}{\left(R + r_0 - \sqrt{R^2 - x^2}\right)^2} - \frac{F_{y1}}{E_s\cdot\pi\cdot r_0^2}\cdot\left(2x_0 + L_s\right)}{\frac{2\cdot F\cdot r_0^2\cdot\int_0^{x_0}\frac{dx}{\left(R + r_0 - \sqrt{R^2 - x^2}\right)^2} - 2\cdot\sigma_{y2}\cdot\pi\cdot r_0^2\cdot x_0}{F - \sigma_{y2}\cdot\pi\cdot r_0^2} + L_s} \tag{3.28}$$

The total strain over the gage section is

$$\varepsilon = \varepsilon_y + \varepsilon_p = \frac{F_{y1}}{E_s\cdot\pi\cdot r_0^2} + \frac{L_1 - L_2 - \frac{2\cdot F}{E_s\cdot\pi}\cdot\int_{x_0}^{x_l}\frac{dx}{\left(R + r_0 - \sqrt{R^2 - x^2}\right)^2} - \frac{F_{y1}}{E_s\cdot\pi\cdot r_0^2}\cdot\left(2x_0 + L_s\right)}{\frac{2\cdot F\cdot r_0^2\cdot\int_0^{x_0}\frac{dx}{\left(R + r_0 - \sqrt{R^2 - x^2}\right)^2} - 2\cdot\sigma_{y2}\cdot\pi\cdot r_0^2\cdot x_0}{F - \sigma_{y2}\cdot\pi\cdot r_0^2} + L_s} \tag{3.29}$$

Since the lower yield strength σ_{y2} is calculated with

$$\sigma_{y2} = \frac{F_{y2}}{\pi \cdot r_0^2}$$

(3.30)

The total strain over the gage section can be finally expressed as a function of total measured displacement ($L_1 - L_2$) and applied force F with a pre-determination of upper and lower yield force (F_{y1} and F_{y2}) at gage section as illustrated in Figure 3-3,

$$\varepsilon = \frac{F_{y1}}{E_s \cdot \pi \cdot r_0^2} + \frac{L_1 - L_2 - \frac{2 \cdot F}{E_s \cdot \pi} \cdot \int_{x_0}^{x_l} \frac{dx}{\left(R + r_0 - \sqrt{R^2 - x^2}\right)^2} - \frac{F_{y1}}{E_s \cdot \pi \cdot r_0^2} \cdot (2x_0 + L_s)}{\frac{2 \cdot F \cdot r_0^2 \cdot \int_0^{x_0} \frac{dx}{\left(R + r_0 - \sqrt{R^2 - x^2}\right)^2} - 2 \cdot F_{y2} \cdot x_0}{F - F_{y2}} + L_s}$$

(3.31)

In summary, after the specimen overall displacement is measured with the laser extensometer system and the specimen force history is determined with the transmitted bar strain signal,

$$F(t) = E_0 \cdot A_0 \cdot \varepsilon_t(t)$$

(3.32)

The specimen strain over the gage section can be determined with

$$\varepsilon = \begin{cases} c' \cdot \dfrac{L_1 - L_2}{L_s} & \text{(Region I)} \\ \dfrac{L_1 - L_2}{L_s} - \dfrac{F}{E_s \cdot \pi \cdot r_0^2} \cdot \left(\dfrac{1}{c'} - 1\right) & \text{(Region II)} \\ \dfrac{F_{y1}}{E_s \cdot \pi \cdot r_0^2} + \dfrac{L_1 - L_2 - \frac{2 \cdot F}{E_s \cdot \pi} \cdot \int_{x_0}^{x_l} \frac{dx}{\left(R + r_0 - \sqrt{R^2 - x^2}\right)^2} - \frac{F_{y1}}{E_s \cdot \pi \cdot r_0^2} \cdot (2x_0 + L_s)}{\frac{2 \cdot F \cdot r_0^2 \cdot \int_0^{x_0} \frac{dx}{\left(R + r_0 - \sqrt{R^2 - x^2}\right)^2} - 2 \cdot F_{y2} \cdot x_0}{F - F_{y2}} + L_s} & \text{(Region III)} \end{cases}$$

(3.33)

For reference, the indefinite integral, $\int \frac{dx}{\left(R + r_0 - \sqrt{R^2 - x^2}\right)^2}$, evaluates to

$$\int \frac{dx}{\left(R + r_0 - \sqrt{R^2 - x^2}\right)^2} =$$

$$\left(\frac{\sqrt{r_0}\, x(r_0 + R)\left(r_0 + R + \sqrt{r_0^2 + R^2}\right)}{R^2 (r_0 + 2R)\left(r_0^2 + x^2 + 2r_0 R\right)} + \frac{\tan^{-1}\left(\dfrac{x(r_0 + R)}{\sqrt{r_0}\sqrt{r_0 + 2R}\sqrt{R^2 - x^2}} \right)}{(r_0 + 2R)^{3/2}} + \frac{\tan^{-1}\left(\dfrac{x}{\sqrt{r_0}\sqrt{r_0 + 2R}} \right)}{(r_0 + 2R)^{3/2}} \right) R^2 r_0^{-3/2}$$

(3.34)

3.4. Typical Stress-Strain Response

Now we use the original strain gage and laser signals shown in Figure 3-2 to determine the specimen stress-strain response. Figure 3-5 shows the specimen force history calculated with Equation (3.32), uncorrected strain history calculated from laser extensometer signals with $c' = 1$ in Equation (2.1), and corrected strain history with Equation (3.33). As shown in Figure 3-5, there exists slight difference between the uncorrected and corrected specimen strains in *Regions I* and *II*. However, it should be emphasized that, although the absolute value of difference between uncorrected and corrected strains was very small in *Region I*, the corrected strain was only 62% ($c' = 0.62$) of the uncorrected strain. This means that the Young's modulus would be significantly underestimated if the specimen strain was not corrected. In *Region II*, the specimen gage section is in plasticity and the elastic deformation of the shoulders (non-gage sections) produced minimal effect on the strain measurement over the gage section. However, in *Region III*, the corrected strain was significantly lower that the uncorrected strain because portion of the shoulders (non-gage sections) has been deformed plastically as shown in Figure 3-6. Figure 3-6 shows the time history of x_0 as defined in Figure 3-4 and corresponding applied force history. In *Regions I* and *II*, the value of x_0 remains zero meaning the whole shoulders (non-gage sections) were in elasticity. However, when the specimen state entered into *Region III*, the value of x_0 was no longer zero, indicating the shoulders (non-gage sections) started into plasticity, and increasing value of x_0 with increasing force indicates that the plastic region became larger and larger while moving outward to the specimen ends. When the specimen failed, a 1.74-mm-long portion over a total 3.18-mm-long shoulder (non-gage section) at each end had been subjected to plastic deformation. In other words, 54.7% of the shoulders had been plastically deformed when the specimen failed. This large plastic region in the shoulders significantly overestimated the failure strain over the gage section. As shown in Figure 3-5, a 19.2% failure strain was measured without correction of specimen gage-section strain. With correction, the failure strain was reduced to 13.5%. This means that the specimen failure strain would be overestimated by 42.2% if the strain correction (Equation 3.33) over the gage section was not applied.

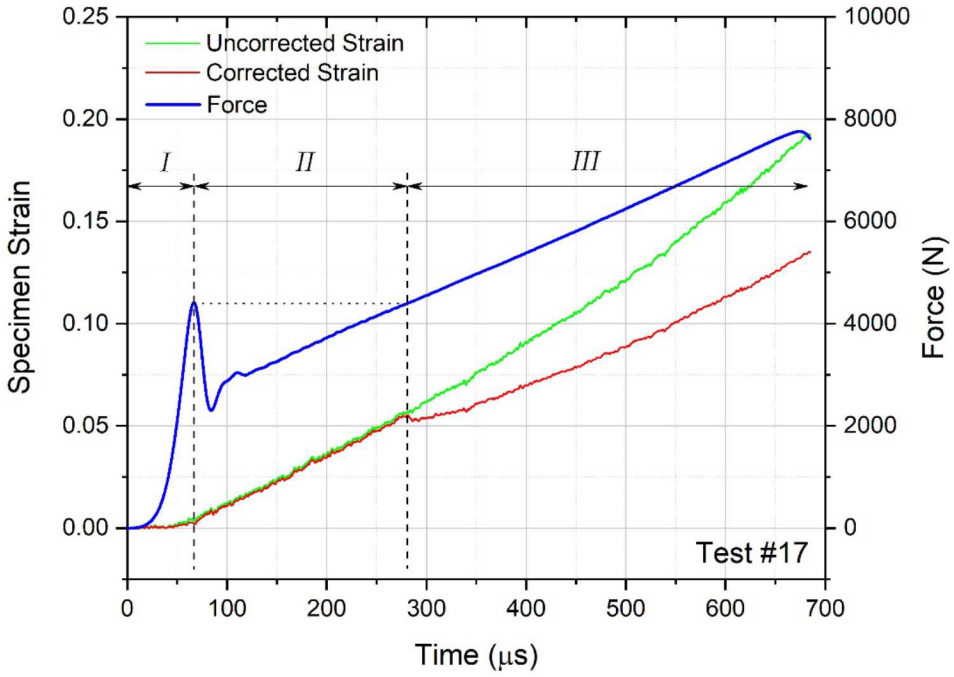

Figure 3-5. Uncorrected and Corrected Specimen Strains over Gage Section

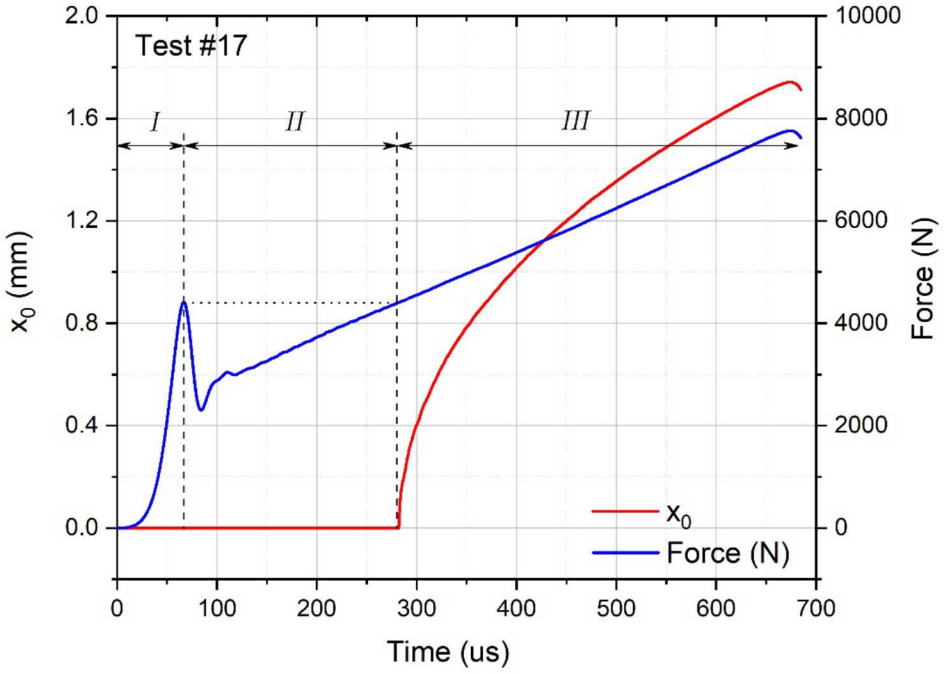

Figure 3-6. Time History of x_0 and Corresponding Force History During Dynamic Loading

As seen Figure 3-5, the shape of specimen strain history was significantly changed after such a correction, which consequently changed the specimen strain-rate history. The strain rate over the gage section was calculated through differentiation of the strain history, the result of which is shown in Figure 3-7. Due to appropriate pulse shaping, the specimen was roughly subjected to a nearly constant strain rate of ~230 s^{-1}. A "dip" was observed to occur at the strains between 5% and 5.5%, which was due to the initiation of plastic region in the shoulder (Figure 3-5). A better pulse shaping would reduce the "dip" but is challenging. Due to the post-test correction process, neither the original laser extensometer signal nor the reflected pulse exactly represents the actual specimen strain or strain rate history, making the experimental design in a "blind" manner with additional iterative process for constant strain rate tests.

The dynamic tensile stress-strain curve from the test is also shown in Figure 3-7. The dynamic tensile stress-strain response is slightly different from quasi-static results shown in the literature. Compared to the quasi-static results, the dynamic tensile stress-strain curve exhibited an upper-lower-yield immediately followed with a linear behavior rather than a plateau Lüders banding that was observed in quasi-static tests. This phenomenon has also been observed by El-Magd et al. [18] on Armco-iron, tempered 42CrV6 steel, pure tantalum, and tungsten alloy at high strain rates on the order of 10^3 s^{-1}. This difference between quasi-static and high rate behavior warrants further detailed investigation in the future.

In a Dropkinson bar test, similar laser extensometer and transmission bar strain gage signals to those shown in Figure 3-2 were obtained. These signals were processed following the same procedure presented above to obtain the tensile stress-strain response of the material at lower strain rates: ~40 and 70 s^{-1} (Table 3-1).

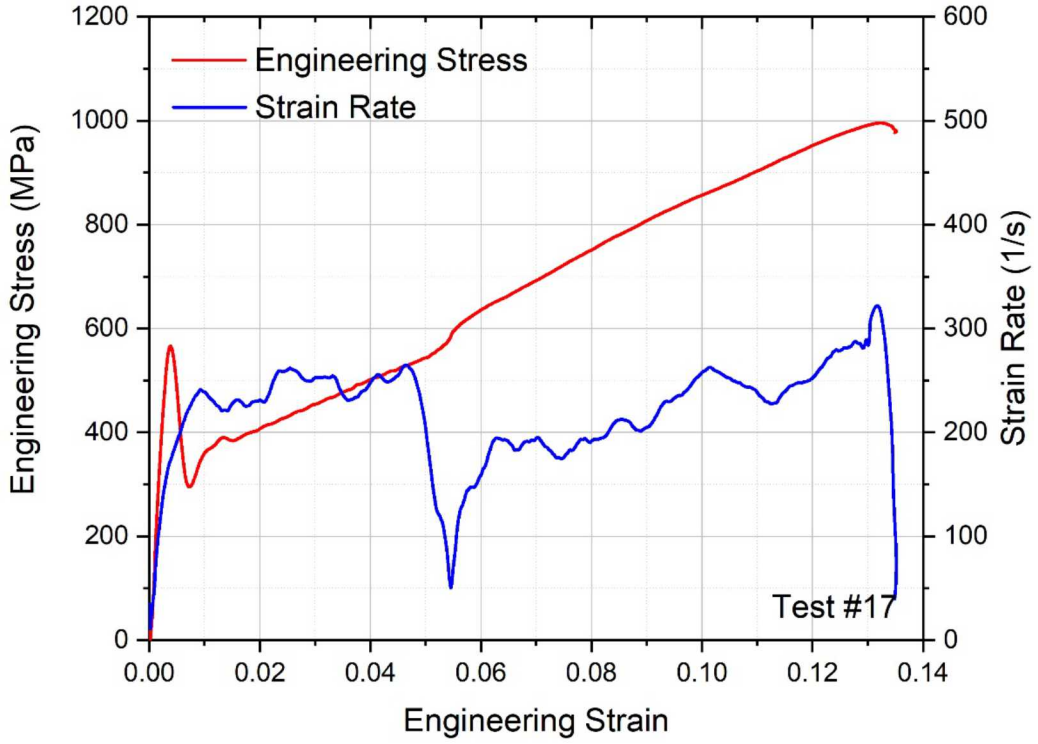

Figure 3-7. Histories of Strain Rate and Engineering Stress in the Specimen

This page left blank

4. EXPERIMENTAL RESULTS

Following the same procedure presented in Section 3.4, the Hiperco 50A was dynamically characterized at different environmental conditions as listed in Table 3-1. The experimental results are presented in this section.

4.1. General Dynamic Tensile Stress-Strain Response

Figures 4-1 – 4-7 show the dynamic tensile stress-strain curves obtained at different environmental conditions. As shown in each figure, 3-5 experiments were repeated at the same condition. All tensile stress-strain curves exhibit very similar response – an initial linear elastic response to an upper yield followed by a Lüders band region and then a nearly linear work-hardening behavior. The upper yield strength and Lüders band region are sensitive to strain rate. The upper yield peaks were observed to be significant at high strain rates (~220 s^{-1}) and became insignificant when strain rate dropped to ~40 s^{-1} that are consistent with previous quasi-static results. The Lüders bands at high strain rates (~220 s^{-1}) showed a hardening feature rather than a plateau that was observed at low strain rates (~40 s^{-1}). The hardening rate seemed independent of strain rate. At similar strain rates, the tensile stress-strain response of the material was observed to be sensitive to temperature as shown in Figures 4-1 – 4-4.

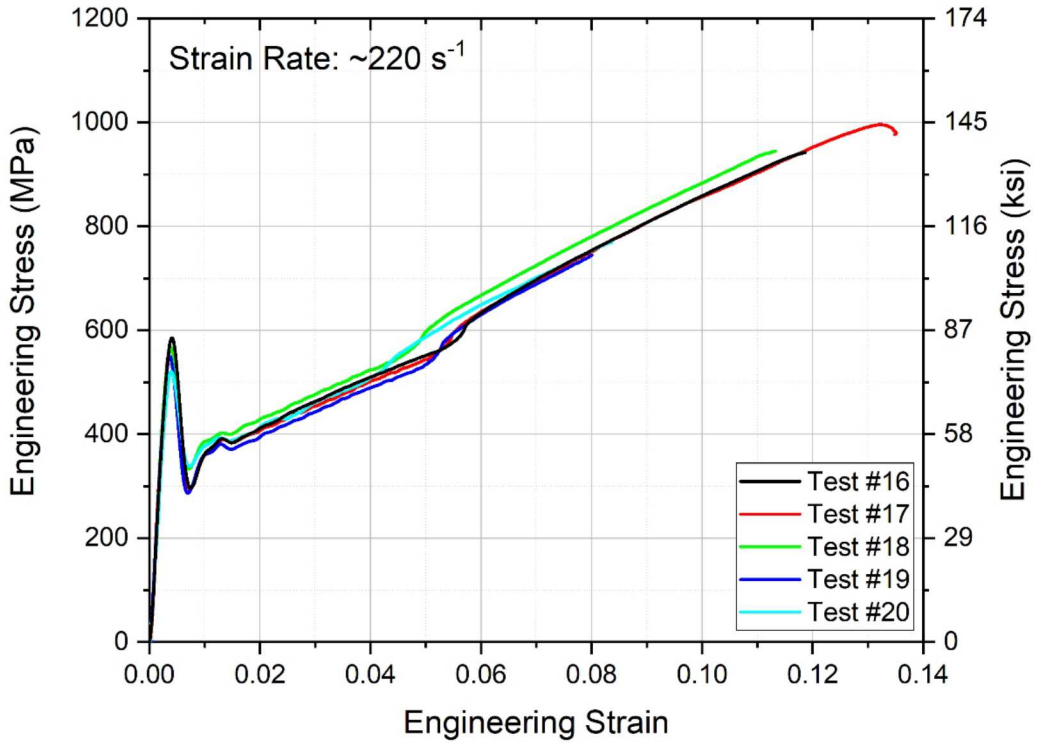

Figure 4-1. Engineering Stress-Strain Curves in Tension at 220 s^{-1}/20°C

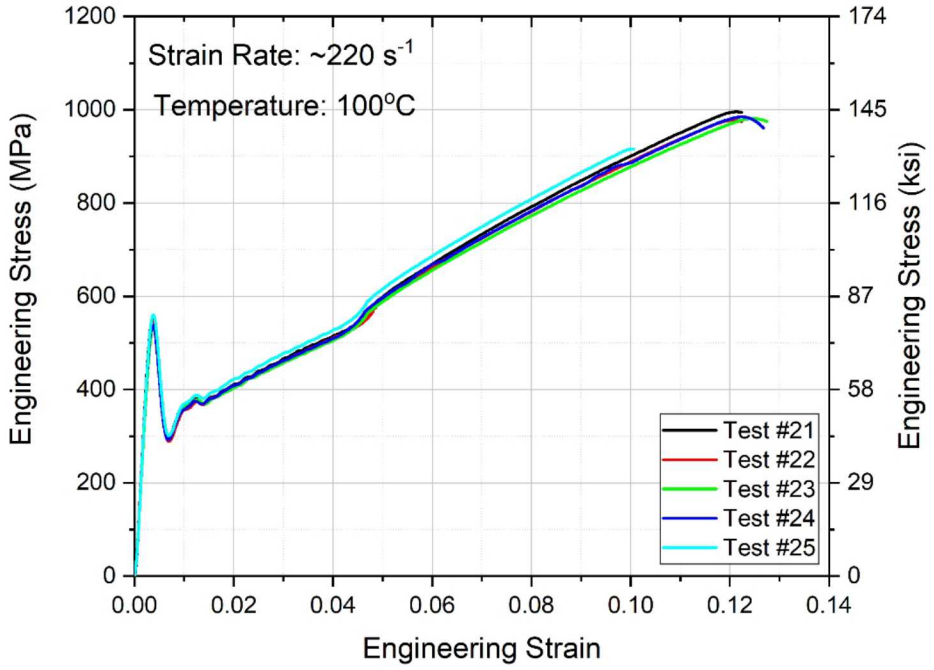

Figure 4-2. Engineering Stress-Strain Curves in Tension at 220 s^{-1}/100°C

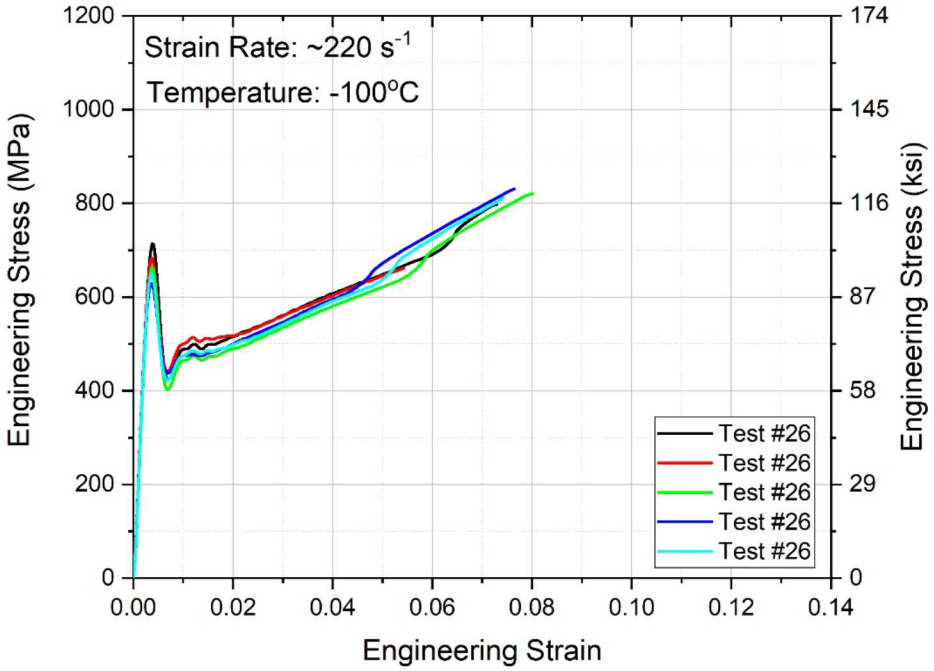

Figure 4-3. Engineering Stress-Strain Curves in Tension at 220 s^{-1}/-100°C

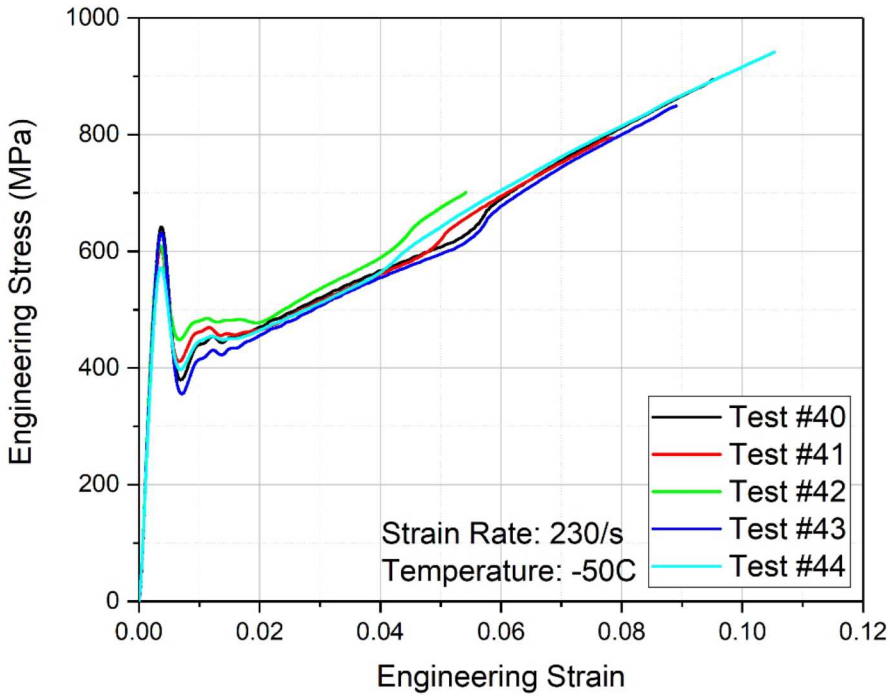

Figure 4-4. Engineering Stress-Strain Curves in Tension at 230 s^{-1}/-50°C

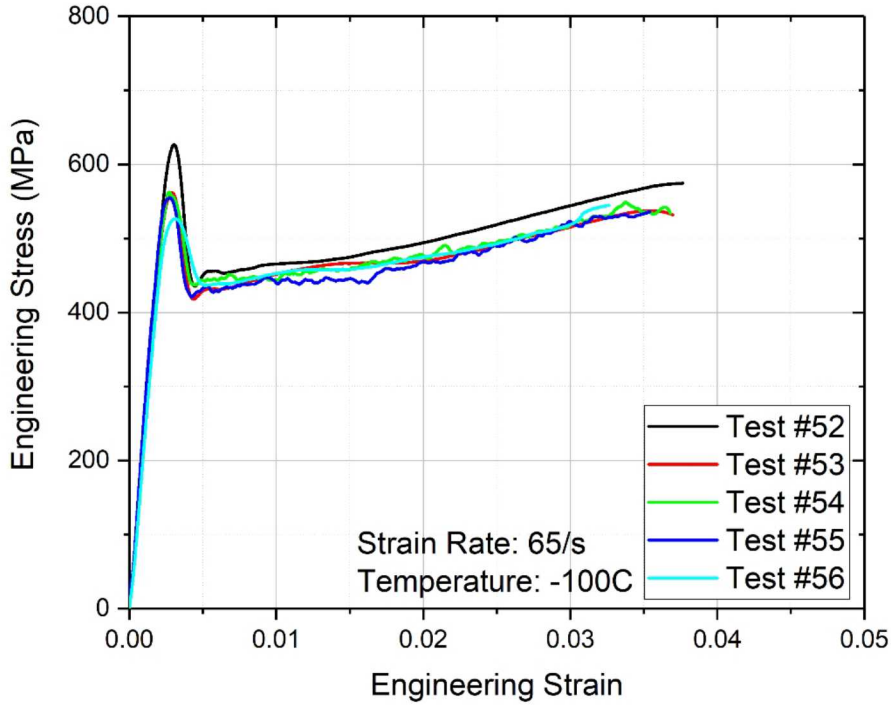

Figure 4-5. Engineering Stress-Strain Curves in Tension at 65 s^{-1}/-50°C

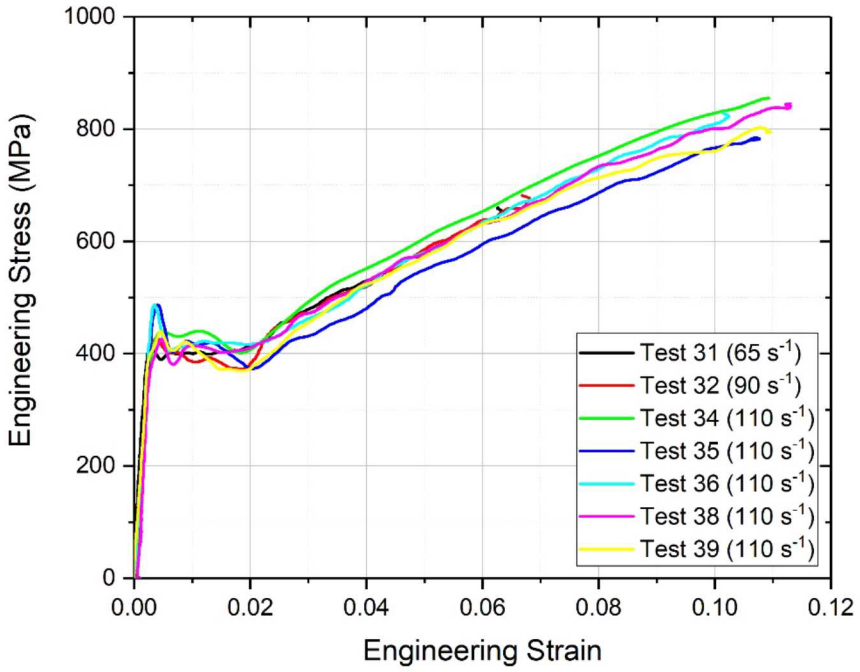

Figure 4-6. Engineering Stress-Strain Curves in Tension at 110 s^{-1}/20°C

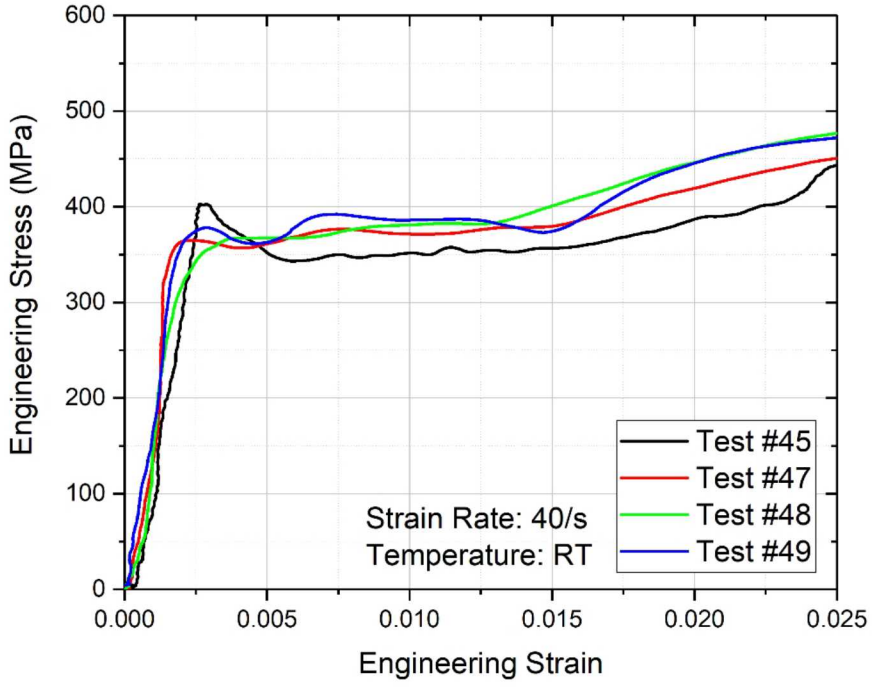

Figure 4-7. Engineering Stress-Strain Curves in Tension at 40 s^{-1}/20°C

Furthermore, the material exhibited a variety of failure strains at different conditions, as summarized in Table 4-1. The stress-strain plots shown in Figures 4-5 – 4-7 do not represent the failure of specimen since the duration of loading was not sufficiently long to break the specimens during the first round of loading. No specimen failure information at these conditions was reliably obtained and is listed in Table 4-1. The ultimate strength at failure is listed in Table 4-1 for available specimens.

Table 4-1. Specimen Ultimate Strength and Failure Strain

Strain Rate (s^{-1})	Temperature (°C)	Specimen #	Ultimate Strength (MPa)	Failure Strain
220	20 (R.T.)	12	942.10	0.1187
		13	995.43	0.1327
		14	944.62	0.1133
		15	744.45	0.0801
		16	768.71	0.0836
		Mean	879.06 ± 114.14	0.1057 ± 0.0229
220	100	17	995.52	0.1214
		18	977.38	0.1206
		19	981.06	0.1246
		20	984.70	0.1224
		21	915.90	0.1006
		Mean	970.91 ± 31.49	0.1179 ± 0.0098
220	-100	22	797.60	0.0729
		23	661.55	0.0543
		24	820.47	0.0801
		25	830.84	0.0765
		26	812.09	0.0742
		Mean	784.51 ± 69.80	0.0716 ± 0.0101
230	-50	36	894.42	0.0951
		37	794.48	0.0785
		38	700.90	0.0542
		39	849.00	0.0891
		40	941.70	0.1053
		Mean	836.10 ± 93.18	0.0844 ± 0.0195

4.2. Strain Rate Effect

The mean room-temperature curves were taken at each strain rate to investigate the effect of strain rate on the tensile stress-strain response of Hiperco 50A alloy, the result of which is shown in Figure 4-8. It is noted that, due to the calculation process, such mean curves shown in Figure 4-8 do not necessarily provide reliable failure strain information. Figure 4-8 also shows a quasi-static tensile stress-strain curve previously obtained [17] as a reference. As shown in Figure 4-7, the upper yield strength significantly increased with increasing strain rate. The stresses during Lüders banding also showed strain rate effect. However, the flow stresses post-Lüders banding seemed to insignificantly depend on the strain rate within dynamic strain-rate range, but were approximately 30% higher than the quasi-static flow stress. The hardening rate was observed to be independent of strain rate from quasi-static to dynamic tests.

Figure 4-9 shows detailed strain rate effects on the upper yield strength and flow stresses at 2% and 5% engineering strains. Note that the strain rate might not have reached the desired value when the specimen was yielded, which means the actual strain rate at yield may be lower than the nominal value. In Figure 4-9, the actual values of strain rate at yield were taken to investigate strain rate effect. In addition, a power law was used to fit the strain-rate effect on the yield strength, whereas linear curve fittings to a logarithm of strain rate were applied to reflect the strain-rate effect on the flow stresses at 2% and 5% engineering strains,

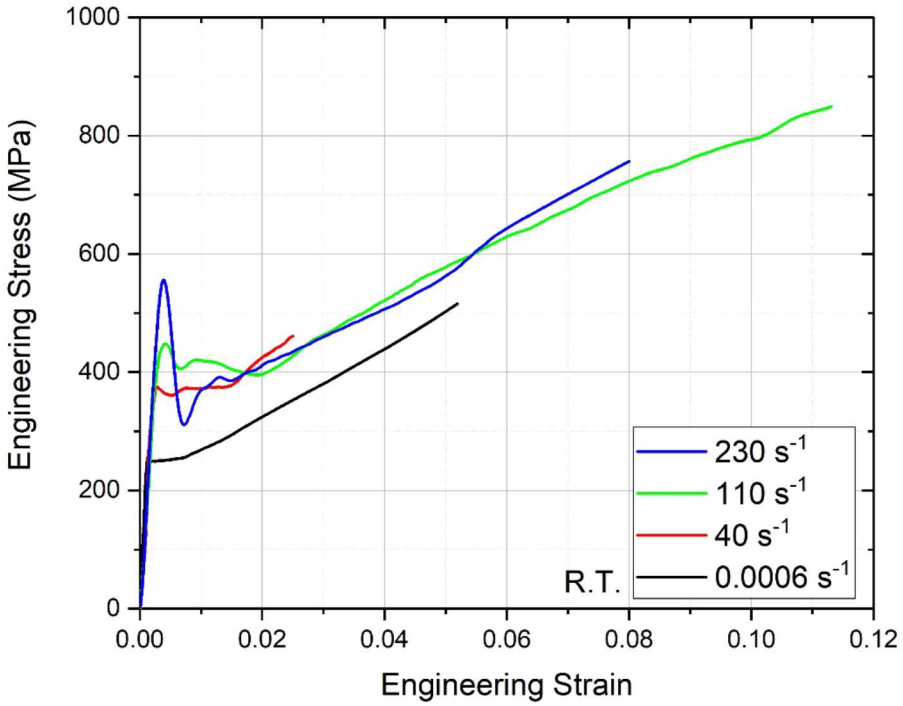

Figure 4-8. Average Tensile Stress-Strain Curves Various Strain Rates (20°C)

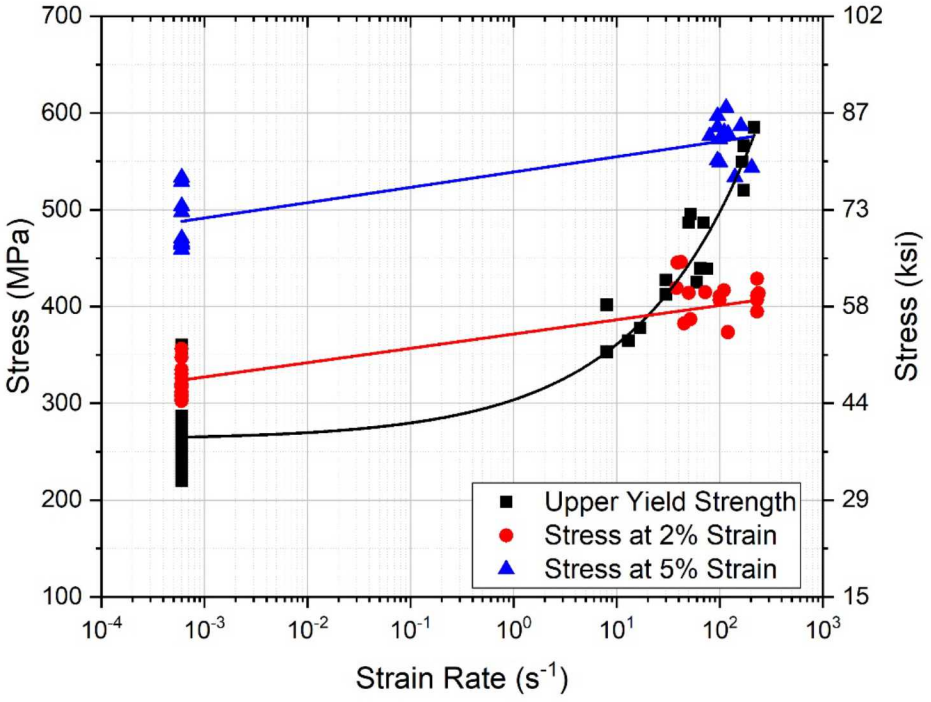

Figure 4-9. Strain Rate Effect at Room Temperature (20°C)

$$\sigma_y = \sigma_{y0} + A_0 \cdot \left(\frac{\dot{\varepsilon}}{\dot{\varepsilon}_0}\right)^n \quad \text{(upper yield strength)} \tag{4.1}$$

$$\sigma = \sigma_1 + A_1 \cdot \log\left(\frac{\dot{\varepsilon}}{\dot{\varepsilon}_0}\right) \quad \text{(flow stress at 2\% engineering strain)} \tag{4.2}$$

$$\sigma = \sigma_2 + A_2 \cdot \log\left(\frac{\dot{\varepsilon}}{\dot{\varepsilon}_0}\right) \quad \text{(flow stress at 5\% engineering strain)} \tag{4.3}$$

where $\sigma_{y0} = 262.56$ MPa, $n = 0.3788$, $A_0 = 2.4739$ MPa, $\sigma_1 = 323.99$ MPa, $A_1 = 14.7733$ MPa, $\sigma_2 = 488.02$ MPa, $A_2 = 15.8241$ MPa, and $\dot{\varepsilon}_0$ is reference strain rate $\dot{\varepsilon}_0 = 0.0006$ s^{-1}.

4.3. Temperature Effect

The mean curves were taken at each temperature but at the same strain rate of (~230 s^{-1}) to investigate the effect of temperature on the tensile stress-strain response of the Hiperco 50A alloy, the results of which are shown in Figure 4-10. The mean curves shown in Figure 4-10 do not represent actual failure strain information. All stress-strain curves shown in Figure 4-10 exhibit very similar profiles, but the flow stress increased with decreasing temperature, although there was little difference in the stress-strain response between 20°C (room temperature) and 100°C. Compared to room temperature, the upper yield strength increased by nearly 18% when temperature dropped to -100°C.

Figure 4-11 shows the detailed temperature effect on the upper yield strength and flow stresses at the engineering strains of 3% and 7%. As seen in Figure 4-11, all followed the same trend but with different offsets. The flow stress exponentially decreased with increasing temperature, which can be generally expressed as

$$\sigma = \sigma_0 + B \cdot e^{-\alpha \cdot \frac{T}{T_0}} \tag{4.4}$$

where $B = 19.3842$ MPa, $\alpha = 0.3704$, T_0 is reference temperature $T_0 = 20^{\circ}C$, and

$$\sigma_0 = \begin{cases} 544.07\ MPa & \text{(at upper yield)} \\ 444.20\ MPa & \text{(at 3\% engineering strain)} \\ 693.53\ MPa & \text{(at 7\% engineering strain)} \end{cases} \tag{4.5}$$

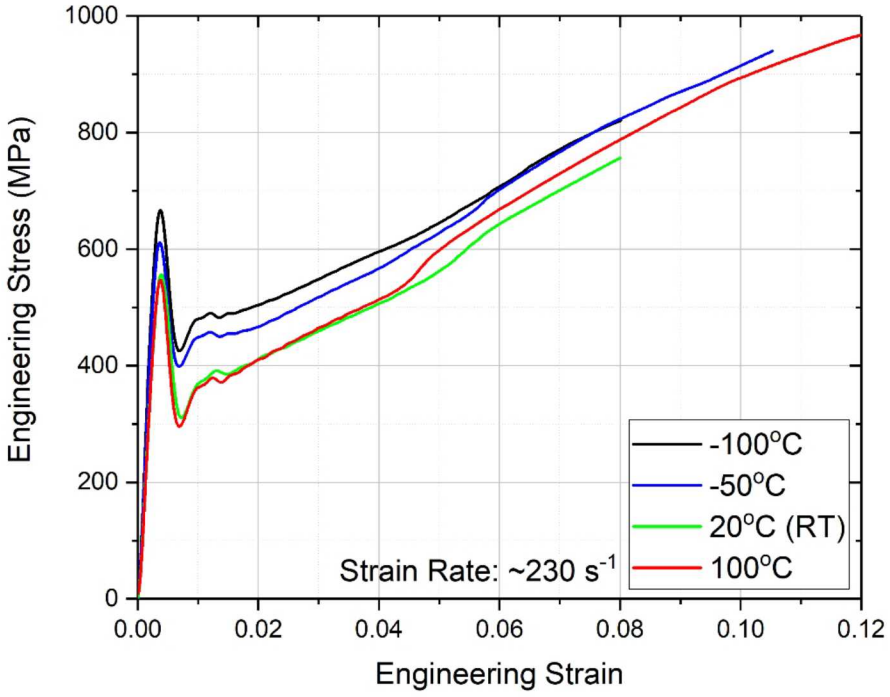

Figure 4-10. Average Tensile Stress-Strain Curves at Various Temperatures (~230 s^{-1})

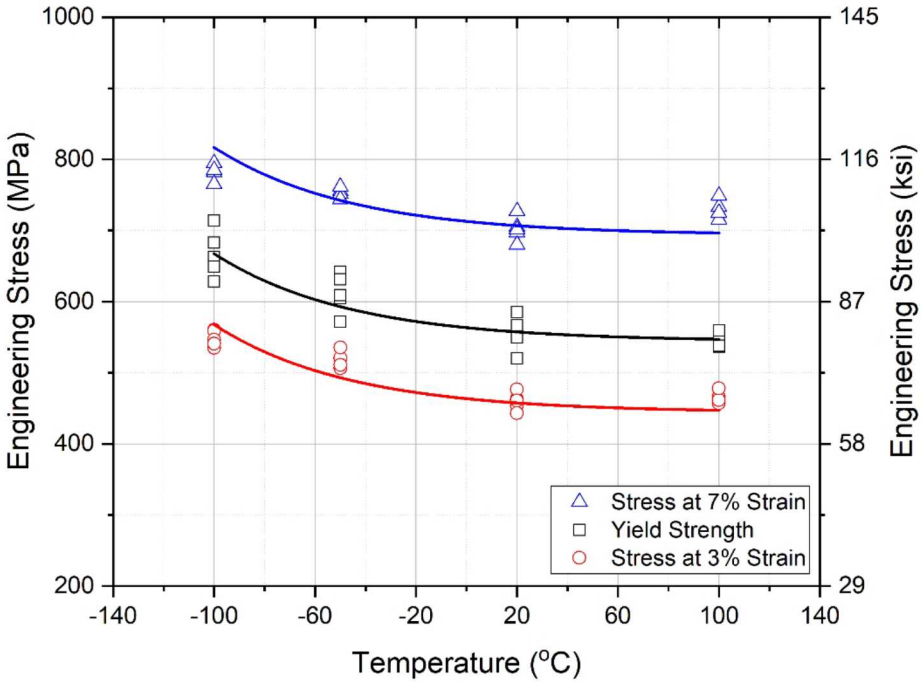

Figure 4-11. Temperature Effect on Yield Strength and Flow Stress (230 s^{-1})

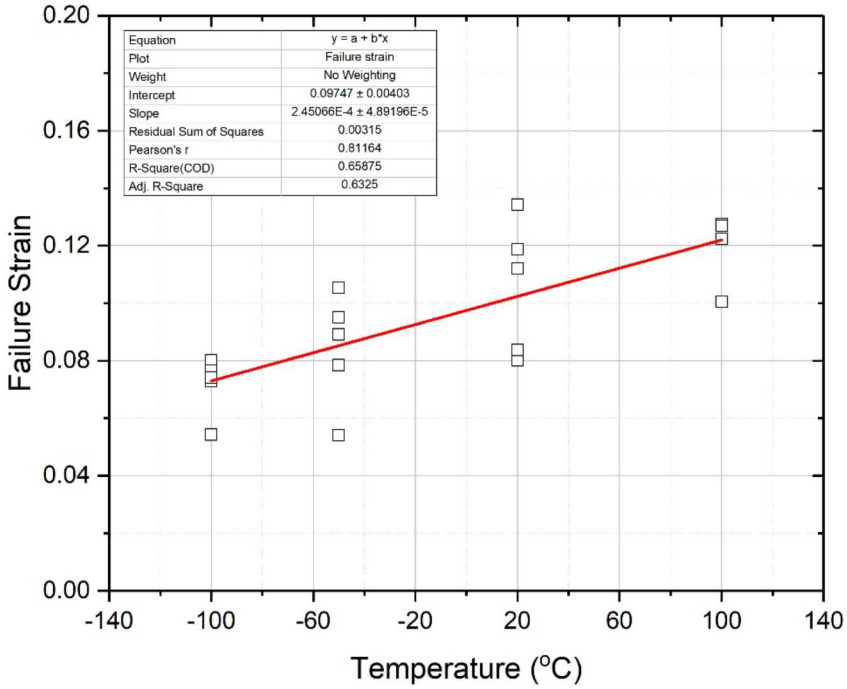

Figure 4-12. Temperature Effect on Failure Strain (230 s^{-1})

Figure 4-12 shows the effect of temperature on failure strain at the same strain rate of ~230 s^{-1}. The failure strain was found to linearly decrease with decreasing temperature, which indicates that the Hiperco 50A alloy became more brittle when temperature dropped. The temperature effect on the failure strain can be described with the following equation,

$$\varepsilon_f = \varepsilon_{f0} + \beta \cdot \frac{T}{T_0} \tag{4.6}$$

where $\varepsilon_{f0} = 0.09747$, $\beta = 0.004902$.

As shown in Figure 4-5, another set of dynamic tests at the low temperature (-100°C) and strain rate of 70 s^{-1} were conducted with the Kolsky tension bar. Note that the specimens did not fail during the first loading. The ends of the stress-strain curves shown in Figure 4-5 do not represent the failure of specimens. At the lower strain rate of ~70 s^{-1} but low temperature of -100°C, the stress-strain curves exhibited significant upper yield peaks but flatter Lüders banding followed by work hardening with similar rates. The average upper yield strength (564 MPa) at this condition (70 s^{-1}/-100°C) was observed to be lower than that (666 MPa) obtained at the same temperature but a higher strain rate (~230 s^{-1}), as shown in Figure 4-11. However, considering standard deviation, this upper yield strength (564 MPa) is consistent with the upper yield strength (547 MPa) obtained at the condition of 230 s^{-1}/100°C, which may indicate some strain rate/temperature superposition for this material.

4.4. Post-test Specimens

In general, the Hiperco 50A alloy exhibited brittle fracture features under dynamic loading. Figures 4-13 and 4-14 show two typical fractured specimens (Specimens #13 and #19 listed in Table 4-1) after dynamic tests. As shown in Table 4-1, the two specimens were tested at the same strain rate but different temperatures. However, the post-test fracture surfaces of both specimens were nearly the same. Both specimens fractured within the gage section but did not show any necking, even at high temperature (100°C). In addition to the fracture surface, some cracks were also observed near the fracture surface. Orange peel deformation was observed to widespread across the gage length. The cross-sections of the specimens still maintained a circular shape after fractured, indicating that the specimens were in-plane isotropic (within the plane perpendicular to the loading direction).

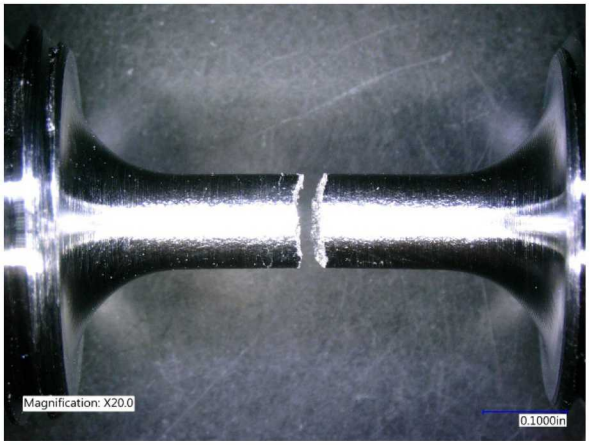

(a) 20x

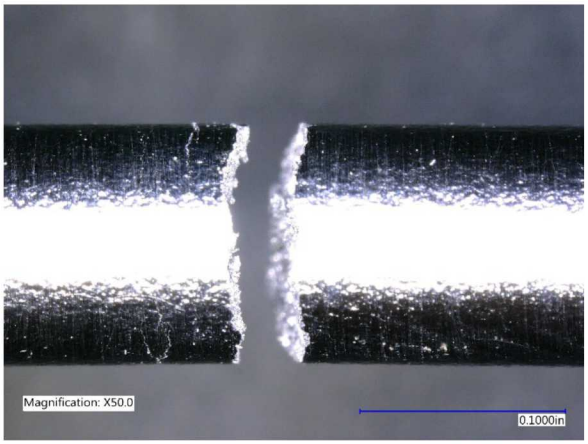

(b) 50x

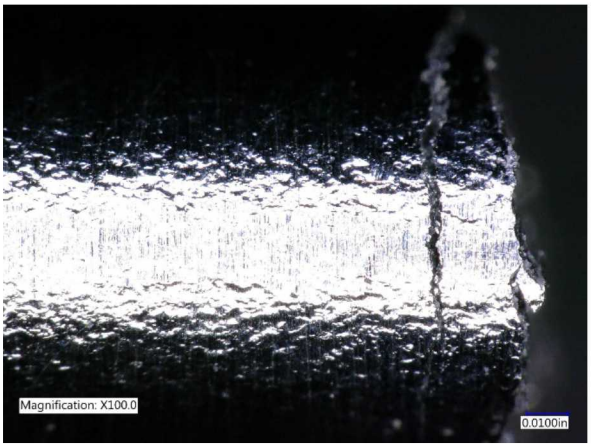

(c) 100x

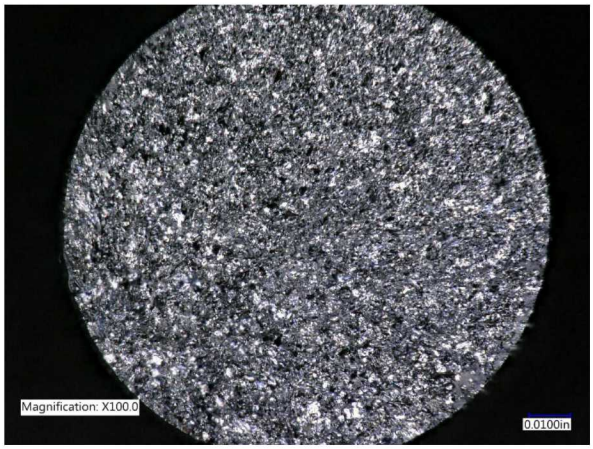

(d) fracture surface

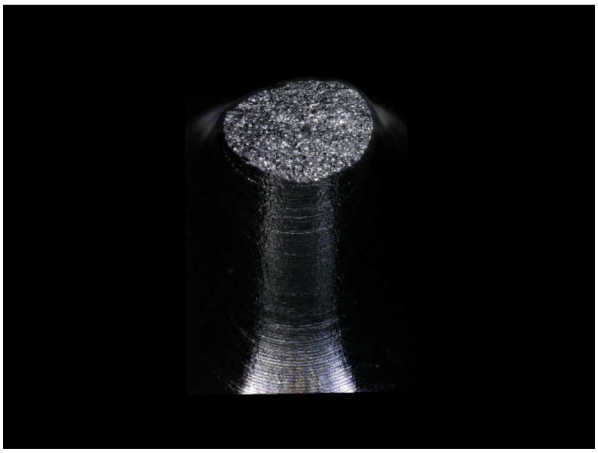

(e) 3D view

(f) 3D view

Figure 4-13. Specimen #13 after Dynamic Test at 220s^{-1}/20°C

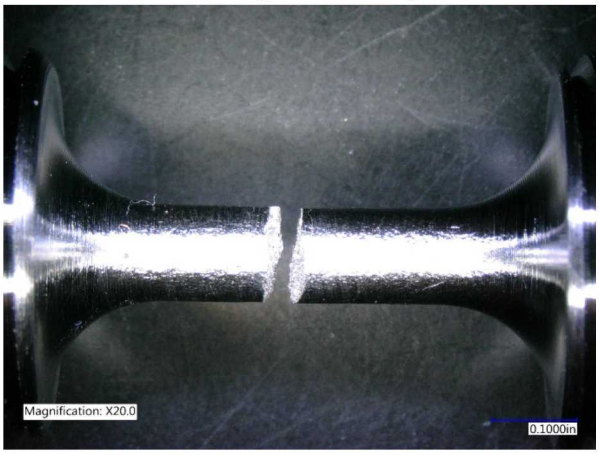

(a) 20x

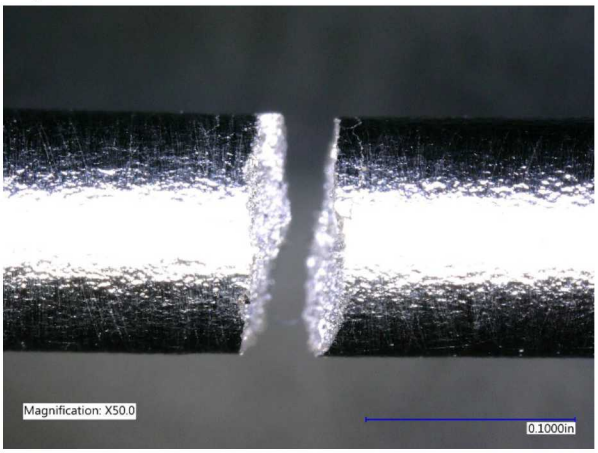

(b) 50x

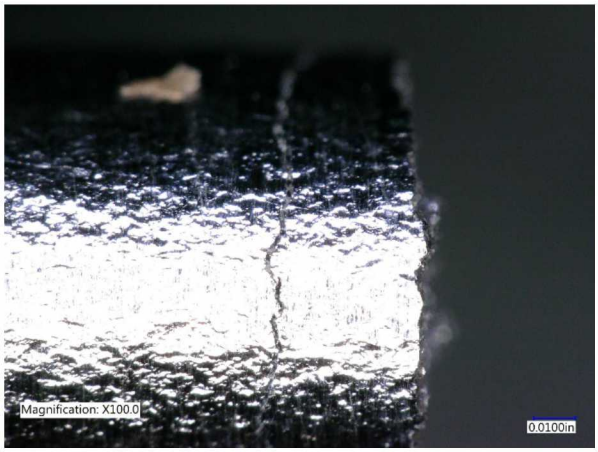

(c) 100x

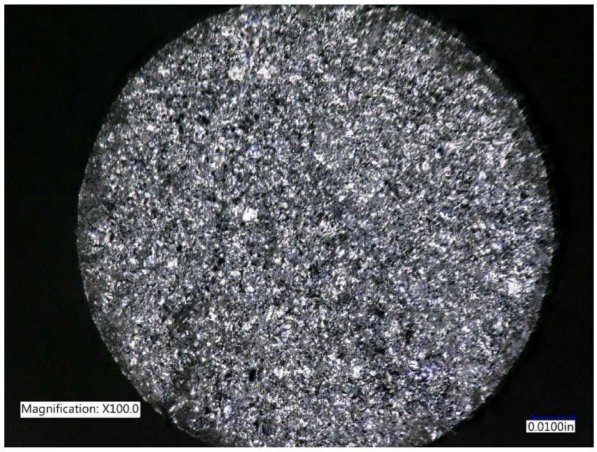

(d) fracture surface

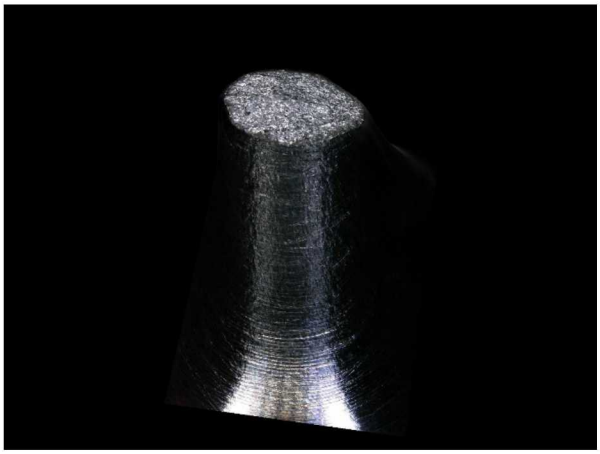

(e) 3D view

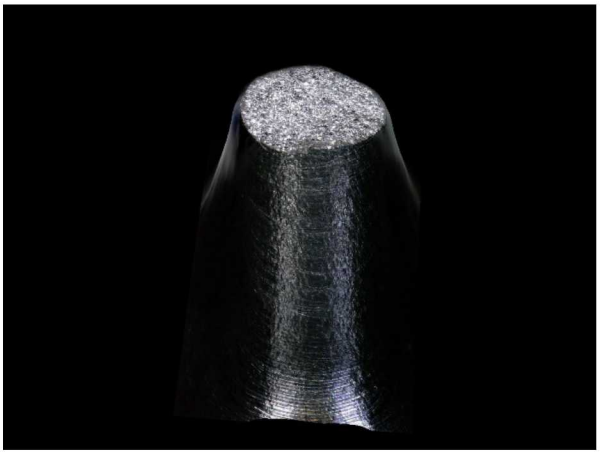

(f) 3D view

Figure 4-14. Specimen #19 after Dynamic Test at 220s^{-1}/100°C

5. CONCLUSIONS

A Kolsky tension bar and a Dropkinson bar were employed to dynamically characterize Hiperco 50A alloy in tension at various strain rates and temperatures. In order to obtain more reliable specimen strain information (particularly the strain at failure), a correction method of specimen strain was developed to calculate the specimen strain over the gage section. Dynamic tensile stress-strain curves of the Hiperco 50A alloy were obtained at strain rates ranging from 40 and 230 s^{-1} and temperatures from -100 to 100°C.

All tensile stress-strain curves exhibited a very similar response – an initial linear elastic response to an upper yield followed by a Lüders banding response and then a nearly-linear work-hardening behavior. The upper yield strength and stress-strain response during Lüders banding are sensitive to strain rate. The upper yield peaks were observed to be significant at high strain rates (~230 s^{-1}). However, when strain rate dropped to ~40 s^{-1}, the upper yield peaks became insignificant and similar to previous quasi-static results. The Lüders bands at high strain rates (~230 s^{-1}) showed a hardening feature rather than a plateau that was observed at lower strain rates (~40 s^{-1}). The hardening rate seemed to be independent of strain rate.

At similar strain rates, the tensile stress-strain response of the material was observed to be sensitive to temperature. The flow stress increased with decreasing temperature, although there was little difference in the stress-strain response between 20°C (room temperature) and 100°C. Compared to the room temperature, the upper yield strength increased by nearly 18% when temperature dropped to -100°C. This upper yield strength obtained at 70 s^{-1}/-100°C is close to that obtained at the condition of 230 s^{-1}/100°C, which may indicate some strain rate/temperature superposition for this material.

The Hiperco 50A alloy exhibited features of brittle fracture in tension under dynamic loading. No specimens showed necking, even at high temperature (100°C). The cross-sections of the specimens maintained a circular shape after fracture, indicating that the specimens were in-plane isotropic (within the plane perpendicular to the loading direction).

REFERENCES

[1] Ren, L., Basu, S., Yu, R.-Hai, Xiao, J.Q., and Parvizi-Majidi, A., 2001, Mechanical properties of Fe-Co soft magnets, *Journal of Materials Science*, 36:1451-1457.

[2] Duckham, A., Zhang, D.Z., Liang, D., Luzin, V., Cammarata, R.C., Leheny, R.L., Chien, C.L., and Weihs, T.P., 2003, Temperature dependent mechanical properties of ultra-fine grained FeCo-2V, *Acta Materialia*, 51:4083-4093.

[3] Fingers, R.T., Coate, J.E., and Dowling, N.E., 1997, Mechanical properties of iron-cobalt alloys for power applications, In: *Proceedings of the 32nd Intersociety Energy Conversion Engineering Conference (IECEC-97)*, July 27-August 2, 1997, Honolulu, HI, Vols. 1-4, pp563-568.

[4] Storch, M.L., Rollett, A.D., and McHenry, M.E., 1999, The effect of mechanical working on the in-plane magnetic properties of Hiperco 50, *Journal of Applied Physics*, 85:6040-6042.

[5] Shang, C.H., Weihs, T.P., Cammarata, R.C., Ji, Y., and Chien, C.L., 2000, Anisotropy in magnetic and mechanical properties in textured Hiperco® FeCoV alloys, *Journal of Applied Physics*, 87:6508-6510.

[6] Song, B., 2017, "Dropkinson bar for intermediate strain-rate testing – design, development, verification, and application," *Sandia Report (OUO)*, SAND 2017-9393.

[7] Song, B., Antoun, B.R., Connelly, K., Korellis, J., and Lu, W.-Y., 2011, Improved Kolsky tension bar for high-rate tensile characterization of materials, *Measurement Science and Technology*, 22:045704.

[8] Song, B., Antoun, B.R., and Jin, H., 2013, Dynamic tensile characterization of a 4330-V steel, *Experimental Mechanics*, 53:1519-1529.

[9] Song, B., Wakeland, P.E., and Furnish, M., 2015, Dynamic tensile characterization of Vascomax® maraging C250 and C300 alloys, *Journal of Dynamic Behavior of Materials*, 1:153-161.

[10]Sanborn, B., Song, B., Thompson, A., Reece, B., and Attaway, S., 2017, High strain rate tensile response of A570 and 4140 steel, *Procedia Engineering*, 197:33-41.

[11] Qiu, Y., Loeffler, C.M., Nie, X., and Song, B., Improved experimental and diagnostic techniques for dynamic tensile stress-strain measurement with a Kolsky tension bar, *Measurement Science and Technology*, 29:075201.

[12] Song, B., and Antoun, B.R., 2012, Pseudo stress response in Kolsky tension bar experiments, *Experimental Mechanics*, 52:525-528.

[13] Nie, X., Song, B., and Loeffler, C.M., 2015, A novel splitting-beam laser extensometer technique for Kolsky tension bar experiment, *Journal of Dynamic Behavior of Materials*, 1:70-74.

[14] Chen, W., and Song, B., 2011, *Split Hopkinson (Kolsky) Bar: Design, Testing, and Applications*, Springer.

[15] Song, B., 2017, Dropkinson bar for intermediate strain-rate testing – design, development, verification, and application, *Sandia Report (OUO)*, SAND2017-9393.

[16] Song, B., Sanborn, B., Heister, J.D., Everett, R.L., Martinez, T.L., Groves, G.E., Johnson, E.P., Kenney, D.J., Knight, M.E., Spletzer, M.A., Haulenbeek, K.K., and McConnell, C., A new apparatus for tensile characterization of materials within upper intermediate strain rate regime, *Experimental Mechanics* (under review).

[17] Greenwood, W.H., and Susan, D.F., 2014, Hiperco mechanical and magnetic properties, Sandia Report (Official Use Only), SAND2014-18371.

[18] El-Magd, E., Scholles, H., and Weisshaupt, H., 1996, Influence of strain rate on the stress-strain curve in the range of Lüders strain, *Steel Research*, 67:495-500.

DISTRIBUTION

Email—Internal

Name	Org.	Sandia Email Address
Charles D. Croessmann	1520	cdcroes@sandia.gov
Randy L. Everett	1528	rlevere@sandia.gov
Darrick M. Jones	1528	dmjones@sandia.gov
Brett Sanborn	1528	bsanbor@sandia.gov
Bo Song	1528	bsong@sandia.gov
Joseph E. Bishop	1556	jebisho@sandia.gov
Adam R. Brink	1556	arbrink@sandia.gov
Cory R. Medina	1556	crmedin@sandia.gov
Steven P. Gomez	1556	spgomez@sandia.gov
Scott J. Grutzik	1556	sjgrutz@sandia.gov
Jeremy L. Guthrie	1556	jlguthr@sandia.gov
Kyle Johnson	1556	kyljohn@sandia.gov
Jonel Ortiz	1556	jonorti@sandia.gov
Shawn M. Dirk	1830	smdirk@sandia.gov
Alexander K. Barr	1831	akbarr@sandia.gov
Collin D. Donohoue	1831	cddonoh@sandia.gov
Jeffrey Rodelas	1831	jmrodel@sandia.gov
Donald F. Susan	1831	dfsusan@sandia.gov
Andrew Kustas	1832	akustas@sandia.gov
Jay Carroll	1851	jcarrol@sandia.gov
Steven Moore	2613	smoore1@sandia.gov
Richard R. Parker	2613	rrparke@sandia.gov
Barry L. Roberts	2613	barrobe@sandia.gov
Sara L. Szarka	2613	slszark@sandia.gov
Patrick J. White	2613	pjwhite@sandia.gov
Francisco Alvarez	2614	falvare@sandia.gov
Jeffrey Dabling	2614	jgdabli@sandia.gov
Sergio Gonzalez	2614	slgonza@sandia.gov
Daniel L. Wilcox	2614	dwilcox@sandia.gov
Jimmy Brown	2615	jbrown@sandia.gov
Rick A. Kellogg	2616	rakello@sandia.gov
Daniel Petersen	2616	depeter@sandia.gov

Name	Org.	Sandia Email Address
Michael P. Sena	2616	mpsena@sandia.gov
Catherine M. Siefert	2616	cmsiefe@sandia.gov
Technical Library	9536	libref@sandia.gov

This page left blank

Sandia National Laboratories

Sandia National Laboratories is a multimission laboratory managed and operated by National Technology & Engineering Solutions of Sandia LLC, a wholly owned subsidiary of Honeywell International Inc. for the U.S. Department of Energy's National Nuclear Security Administration under contract DE-NA0003525.